5-16-2003

Microgmagnetics Study of "Seed" Induced Incoherent Magnetic Reversal in a Cobalt Element Array

Hanning Chen
University of New Orleans

MICROMAGNETICS STUDY OF "SEED" INDUCED INCOHERENT MAGNETIC REVERSAL IN A COBALT ELEMENT ARRAY

A Thesis

Submitted to the Graduate Faculty of the
University of New Orleans
in partial fulfillment of the
requirments for the degree of

Master of Science
in
The Department of Chemistry

by

Hanning Chen

B.S., University of Science and Technology of China, 1999

May 2003

To Those I Love

And

To Those Who Love Me

ACKNOWLEDGMENTS

The author is extremely grateful to Dr. Scott L. Whittenburg for his inspiration, guidance and support throughout this research and preparation of this thesis. Also I would like to thank Dr. Edwin D. Stevens and Dr. Kevin J. Boyd for serving on the examination committee and helpful suggestions.

Advanced Material Research Institute (AMRI) provided the financial support for this research through the Louisiana Board of Regent with Contract No. NSF/LEQSF(2001-04)-RII-03.

My appreciation also goes to all of the members in Dr. Whittenburg's group, including Dr. Nicholas Patrick, Dr. Ngocnga Dao and Mr. Zhidong Zhao, for their kind helps.

Finally, I thank my parents, my grandfather and my finacee Yuanyuan Wang for their love, understanding and support.

TABLE OF CONTENTS

LIST OF FIGURES

ABSTRACT

A stochastic dynamic micromagnetics code using the LLG equation has been developed and applied to study the "seed" induced magnetic reversal of a cobalt element array. The spin orientation of the "seed" element is chosen to be antiparallel to the spin orientation of the first element in the array producing a domain wall that is stabilized by the strong crystalline anisotropy and exchange interactions of cobalt. By exposing the element array to an applied magnetic field for a specific time, the domain wall moved along the easy axis and was pinned at a specific position. In this manner, the portions of the element array to be switched could be controlled arbitrarily and information can be stored in the array in terms of the total magnetization of the array. The effects of the magnitude of applied field, the cutting area and the cellsize of the element array were also studied.

CHAPTER ONE: INTRODUCTION

1. Introduction to Magnetism:[1]

It has been claimed that the Chinese people used the compass three thousand years ago and the Greek people applied the power of magnetite to attract iron sometime before 600 B.C. But, the origin of magnetism remained as a puzzle until the seventeenth century when British scientist William Gilbert (later the physician to Queen Elizabeth I of England) in his great publication <<De Magnete—on the Magnet>> gave the first rational explanation to the mysterious ability of the compass needle to point north-south: the Earth itself is a magnet! Between 1785 and 1791, French scientist Charles Augustin de Coulomb investigated the forces between the magnetic poles, known as Coulomb's Law. The results were presented in the seven papers submitted to Academie des Sciences. His remarkable results formed the starting point of a treatise on magnetism.

Coulomb found that there were two types of poles, called positive and negative. Positive and negative poles always occur in pairs, isolated magnetic poles have never been observed in nature. Such a pair is called a dipole. Since we can assume that there are "free" magnetic poles on the ends of the dipole, the magnetic moment of a dipole is defined as

$$\vec{m} = \mu\vec{d}\,, \qquad \text{(Eq. 1.1)}$$

where μ is the pole strength and $\vec{d}$ is a vector pointing from the negative pole to the positive pole. Usually the magnitudes and directions of the magnetic moments in a substance are different, the magnetization of a substance is defined as

$$\vec{M} = \oint_r \vec{m}(r) d^3 r \,, \qquad \text{(Eq. 1.2)}$$

where $\vec{m}(r)$ is the magnetic moment at point r.

It is found that a magnetic moment can experience an applied force in a region of space. The applied force can be generated by electric currents or by other magnetic moments. The region of space is called the magnetic field. The force acting on the magnetic pole μ by magnetic filed $\vec{H}$ is

$$\vec{F} = \mu \vec{H} \,. \qquad \text{(Eq. 1.3)}$$

Since both of the poles in a magnetic moment are acted upon by the forces, a torque arises as shown by Fig. 1.1. The moment of the torque is

$$\vec{L} = \vec{m} \times \vec{H} \,. \qquad \text{(Eq. 1.4)}$$

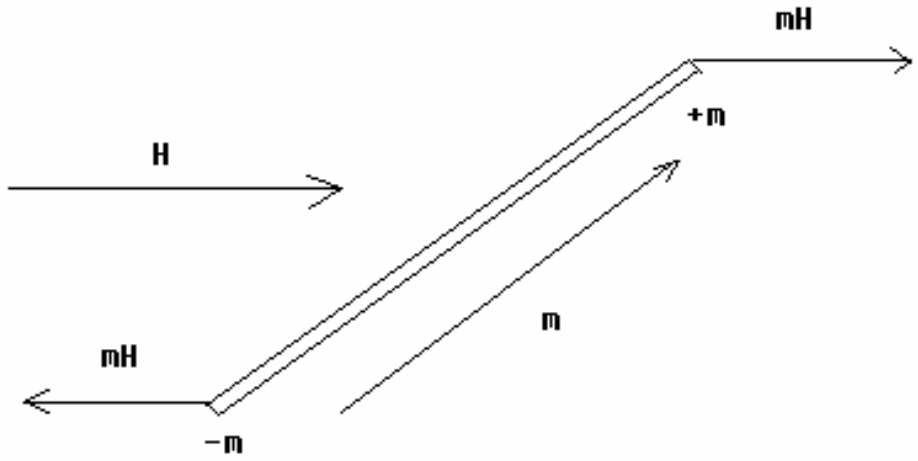

FIG. 1.1 A magnetic moment under the action of a torque in a magnetic field

2. Introduction to Ferromagnetism:

Since the movement of the electron along its orbital produces a closed electric current, which can generate a magnetic moment, any unpaired electron produces a magnetic moment. Based on the different coupling interactions between the magnetic moments in the substance, there are two important classifications. If the coupling forces the neighboring magnetic moments to line up parallel with each other, the substance is said to be ferromagnetic.[2] If the neighboring magnetic moments are aligned antiparallel, the substance is antiferromagnetic.[3] Because of their important applications in electronic signal generation and detection, spin transition and information recording, a lot of research has been conducted on ferromagnetic materials.

A ferromagnetic material can be subdivided into magnetic domains.[4] The magnetization inside each domain is relatively uniform due to the strong coupling interactions between the neighboring magnetic moments, but varies from one domain to another. With the development of modern experimental techniques, detailed images of the domain structure have been observed. The interfaces between two domains are known as domain walls.[5-9] The thickness of the domain wall is mainly determined by an optimal energy requirement because a certain mount of energy is consumed in creating a domain wall.

Although the magnetizations of these domains are stable, ferromagnetism can disappear due to the thermal agitation when the temperature of the material is above a critical temperature. The critical temperature is called the Curie temperature.[2] The ferromagnetism of a ferromagnetic material should be studied below the Curie temperature. Only a few metals exhibit ferromagnetism, including Nickel, Iron and Cobalt. Most of the ferromagnetic materials are ionic compounds and alloys, such as EuO, $BaFe_{12}O_{19}$ and permalloy (80% Ni and 20% Fe).

3. Interactions in the Ferromagnetic Materials:

There are five interactions usually considered in modeling ferromagnetic materials. They are exchange, anisotropy, zeeman, magnetostatic and thermal fluctuation interactions. [10] The exchange interaction is a quantum mechanical effect. The exchange Hamiltonian of a given atom i with its neighbors is

$$\mathrm{H} = -2\sum_{j} J_{ij} S_i \bullet S_j , \qquad \text{(Eq. 1.5)}$$

where S_i is the total spin of the atom i and J_{ij} is the exchange integral of spin i and j. Since J_{ij} is positive for ferromagnetic materials, the parallel alignment of spins is favored by the exchange interaction. In some ferromagnetic materials, the spins are found to lie along certain crystallographic axes due to the asymmetry of the crystal structure. Those interactions are called crystalline anisotropy or anisotropy interactions. Due to different ways of symmetry breaking, there are three kinds of anisotropy interactions. They are uniaxial, cubic and high-order anisotropy. It is found that the spins can interact with the applied external magnetic field. These interactions were

named after Pieter Zeeman who discovered them. The zeeman interactions always try to force the spins to point along the applied field. The magnetostatic interactions are originated from the dipole-dipole interactions, which can be described as

$$H(\vec{r}) = \frac{1}{\mu_0}\left[\frac{3\vec{r}(\vec{r}\cdot\vec{m})}{r^5} - \frac{\vec{m}}{r^3}\right], \qquad \text{(Eq. 1.6)}$$

where μ_0 is the magnetic permeability of a vacuum**,** $\vec{m}$ is the acting spin and $\vec{r}$ is the vector connecting the two spins. From this equation, we can see that the magnetostatic interactions decrease gradient in magnetization. Modeling temperature effect in ferromagnetism had been omitted by researches until in 1963 William F. Brown used the fluctuation-dissipation theorem [11,12] to show how the temperature effects could be expressed as a random magnetic field.

During the relaxation period in ferromagnetic materials, the five interactions compete with each other to adjust the orientations of the spins. Finally, an equilibrium state will form which is a stable configuration of the spins. So, the magnetic properties of ferromagnetic materials are a result of these five competing interactions.

4. Introduction to Micromagnetics:

With advances in technology, the size of ferromagnetic elements used in magnetic storage has decreased dramatically from centimeter to micrometer and even to nanometer length scales. At lengths under a micrometer, macroscopic magnetic theories are not able to describe the behavior of the ferromagnetic material. A theory called micromagnetics,[13] was developed by William F. Brown to understand the magnetism on the small-length scale. In the theory of micromagnetics, a magnetic pattern was

composed of the magnetization vectors $M(\vec{r})$ defined over the entire material body. Since a magnetization vector can assume different orientations, each magnetic pattern has a free energy $G(M(\vec{r}))$. If an external magnetic field is applied, the free energy is denoted as $G(M(\vec{r}), H_a)$. The stability condition for equilibrium states that should be fulfilled at each magnetization vector $\vec{M}(r)$ inside the material body is

$$\vec{M}(r) \times \vec{H}_{eff}(r) = 0 \text{ ,} \qquad \text{(Eq. 1.7)}$$

where $\vec{H}_{eff}(r)$ is the effective field at point r. On the surface of the material, the boundary condition is

$$\vec{M}(r) \times \frac{\partial \vec{M}(r)}{\partial n} = 0 \text{,} \qquad \text{(Eq. 1.8)}$$

where $\frac{\partial \vec{M}(r)}{\partial n}$ indicates the derivative in the outside direction normal to the body surface. To approach the equilibrium states, the energy minimization has to be carried out in the infinite-dimensional space of all possible magnetic patterns. To avoid the nontrivial mathematical and physical difficulties, the time evolution for the magnetization moments can be described by the Landau-Lifshitz-Gilbert (LLG) equation

$$\frac{\partial \vec{M}(r)}{\partial t} = \gamma_L \vec{M}(r) \times \vec{H}_{eff} - \gamma_L \alpha \vec{M}(r) \times (\vec{M}(r) \times \vec{H}_{eff}) \qquad \text{(Eq. 1.9)}$$

where γ_L is the gyromagnetic ratio and α is the phenomenological damping coefficient. The first term on the right side of the equation represents the precessing of $\vec{M}(r)$ with $\vec{H}_{eff}$ and the second term represents the dissipative relaxation of $\vec{M}(r)$ to $\vec{H}_{eff}$ toward equilibrium.

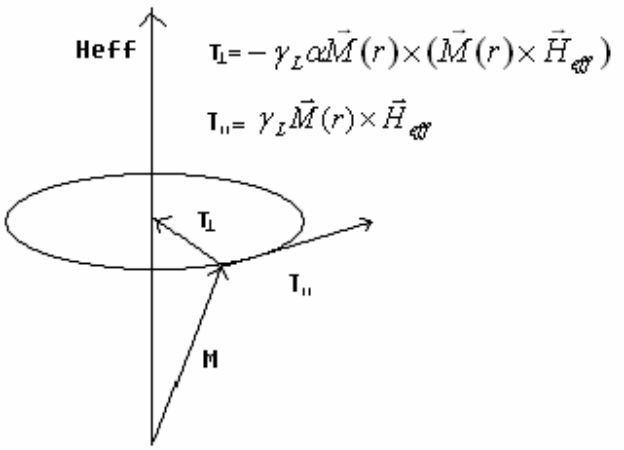

FIG 1.2 Interpretation of Eq. 1.9

When $\frac{\partial \vec{M}(r)}{\partial t} = 0$, both of the equilibrium conditions are fulfilled.

5. Patterned Magnetic Materials and Information Recording:

In the past ten years, a new technology for patterning magnetic layers into a regular matrix of dots has been developed.[14] Because of their possible application as logic gates, [15,16] field sensors[17] and ultra-high density storage media,[18,19] patterned magnetic materials have been extensively studied experimentally[20,21] and theoretically[22,23]. In conventional magnetic recording media, such as that found in the hard disk installed in every modern computer, the magnetic film was sputtered with many single domain grains in which the orientation of the magnetization of the grains is randomly distributed in the plane. To achieve a significant signal to noise ratio, over 100 grains each with lateral size 10 nm are required for one bit of information. The

storage density limitation of $1bit/(100nm \times 100nm) = 10^{10} bit/cm^2$ is expected to be reached within ten years. Although the pattered magnetic recording technology can increase the storage density by separating the bit dots and making only two well defined magnetization states available to the bit dots, the lateral size of the bit dots is still required to be large enough to resist the superparamagnetic effect. If the size of the bit dots is too small, thermal agitation can flip the magnetization states. The superparamagnetic phenomena can make stored information thermally unstable. Since the information must be handled bit by bit, the operation time spent at locating bits and moving magnetic read heads is the bottleneck of conventional disk media. Another disadvantage is the expensive cost for the necessarily small size of the magnetic read heads.

6. Magnetic Domain Wall and its Propagation:

A Domain wall is formed at the interface between the two domains with different magnetization vectors. Domain walls have been observed by magnetic force microscopy and magnetoresistance measurement.[24,25] The magnetization varies in the domain wall, changing from the direction of one of the two neighboring domains to another. So far, many studies have been conducted on "spin" valves by applying different electrical resistivities between two materials with or without the domain walls.[26,27] During the magnetic reversal, the domain wall can propagate in the material. The propagation of a magnetic domain wall in a submicro magnetic wire was observed and the velocity was determined at $77k$.[28] Two different magnetic reversal

mechanisms for domain walls have been reported, one is coherent rotation[29] and the other is incoherent rotation.[30] For the first mechanism, all the spins rotate coherently and act as a single domain. For the second mechanism, the spins rotate semi-independently. In Ref.16, a domain wall was injected easily into a magnetic material and the domain wall was relatively stable after propagation even at room temperature. This study suggests a new way to store information in the domain walls rather than in the single domains as the conventional magnetic storage.

7. Information Storage Strategy by Domain Wall:

In this study, we will examine a novel method for storing information via the position of a domain wall in a magnetic element array. Initially, the domain wall is generated at the interface of two cobalt array elements both initially saturated but with antiparallel spin orientation. Then an external magnetic field with magnitude close to the crystalline anisotropy field is applied along the easy axis of the array elements to propagate the domain wall. Because the final position of the domain wall is determined by the duration of the applied field and the domain wall is very stable after releasing the applied field, the information can be stored in terms of the total magnetization of the element arrays. The inexpensive, magnetically hard, uniaxial anisotropy material Cobalt is a good candidate for the new strategy and is used in this study. Advantage of this method over conventional magnetic storage method will be analyzed and discussed.

CHAPTER TWO: COMPUTATIONAL MODEL

1. Theory of Micromagnetics:

In the theory of micromagnetics, any ferromagnetic material can be subdivided into many magnetic cells. The shape of the cells can be arbitrary, but for convenience of computer programming, most of the micromagnetics calculations were done with cubic cells, as were all calculations in this thesis. The volume sizes of the cells can be different too, but they should be small enough to avoid the underestimation of some interactions in the ferromagnetic material, and big enough to avoid unnecessarily long calculation times. For most ferromagnetic material, the cell size falls into several nanometers. In each cell, the magnitude of magnetization is assumed to be constant while the orientation changes by the guidance of Landau-Lifshitz-Gilbert (LLG) equation under the effect field applied on it. The magnitude of the magnetization in unit volume is defined as saturated magnetization M_s. For convenience, the magnetizations in the cells are called spins.

There are five contributions to the effect field: exchange, anisotropy, zeeman, magnetostatic and thermal stochastic. For each spin, since each of the five local fields may vary with time due to the change of spin configuration or changes in the applied field, the effective field is a function of time. If the applied field changes slowly or does

not change at all, the spins will relax to an equilibrium state in which the effective field on each spin minimizes the torque and the energy.

2. Effect Field $\vec{H}_{eff}$ Calculation:

a. Exchange Field $\vec{H}_{ex}$:

Although there are many strategies to calculate the exchange field $\vec{H}_{ex}$ **,** the three dimensional six-neighbour strategy is assumed in all of the calculations in this thesis. The exchange field $\vec{H}_{ex}$ is expressed as

$$\vec{H}_{ex} = \frac{2A_i}{M_s^{\,2}} \sum_{i=1}^{6} (\Delta\vec{m}_{ix} + \Delta\vec{m}_{iy} + \Delta\vec{m}_{iz}), \qquad \text{(Eq. 2.1)}$$

where A_i is the exchange constant which depends on the magnetic materials, $\Delta\vec{m}_{ix}$, $\Delta\vec{m}_{iy}$ and $\Delta\vec{m}_{iz}$ are the gradients of the reduced spin vector and the sum is over the neighboring cubic-cell spins.

b. Anistropy Field $\vec{H}_{an}$:

I. Uniaxial Anistropy:

In a uniaxial anistropy material, only a single spatial direction called the uniaxial axis or easy axis controls the anisotropy energy. The strength of the anisotropy field is

$$\left|\vec{H}_{an}\right| = \frac{2|K_1|}{\mu_0 M_s}, \qquad \text{(Eq. 2.2)}$$

where K_1 is the anisotropy constant, a material parameter. When $K_1 > 0$, the anisotropy field forces the spins to lie along the uniaxial axis. When $K_1 < 0$, the minimum anisotropy energy corresponds to spins pointing anywhere in the plane perpendicular to the uniaxial axis. This situation is described by the term easy-plane anisotropy.

II. Cubic Anistropy:

There are three easy axes in the cubic anisotropy. The magnitude of the anisotropy field in each of these three directions is

$$\left|\vec{H}_{an}\right| = \frac{4}{3}\frac{|K_1|}{\mu_0 M_s} \quad . \qquad \text{(Eq. 2.3)}$$

The cubic anisotropy typically originates from spin-lattice coupling in cubic crystals.

c. Zeeman Field $\vec{H}_{ze}$:

The Zeeman field is just the applied external field, therefore

$$\vec{H}_{ze} = \vec{H}_{ex} \quad . \qquad \text{(Eq. 2.4)}$$

d. Magnetostatic Field $\vec{H}_{de}$:

The magnetostatic field is due to the magnetic diple-dipole couplings. Since dipole-dipole coupling is a long-range effect, magnetostatic interaction between any

pair of the spins in the sample should be included. For n spins, there are $\frac{n(n-1)}{2}$ pairs. Usually there are hundreds, sometimes, even thousands of spins in a micromagnetic calculation. If the conventional direct dipole-dipole algorithm is used, the computational time for the magnetostatic field will be proportional to n^2. This method becomes extremely expensive, impractical and unacceptable for any reasonable number of spins. Several advanced algorithms, such as Fast Fourierm Transform (FFT), Fast Multipole Method (FMM) and Multigrid Method (MM) have been developed to improve the efficiency of the calculation of dipole-dipole interactions. Although both of the FMM and MM methods can decrease the time-complexity to O(n) , some truncation errors are also introduced. Therefore FFT method with the time-complexity $\mathrm{O}(n\log_2 n)$ was used in this thesis.

Fast Fourierm Transform (FFT) Algorithm:[31]

The magnetostatic field observed at a point specified by indices i, j, k can be expressed as

$$\vec{H}_{de}(i,j,k) = \sum_{l}\sum_{m}\sum_{n}\kappa_{pq}(l,m,n)\vec{M}(i-l,j-m,k-n), \qquad \text{(Eq. 2.5)}$$

where $\kappa_{pq}(l,m,n)$ is the magnetostatic tensor which describes the contribution of the spin M in the cell specified by indices $i-l$, $j-m$ and $k-n$. The analytical form of tensor $\kappa_{pq}(l,m,n)$ is

$$\kappa_{11}(l,m,n) = \frac{M_s}{4\pi}\frac{(2l^2-m^2-n^2)}{(l^2+m^2+n^2)^5},$$

$$\kappa_{12}(l,m,n) = \frac{M_s}{4\pi}\frac{3lm}{(l^2+m^2+n^2)^5},$$

$$\kappa_{13}(l,m,n) = \frac{M_s}{4\pi}\frac{3\ln}{(l^2+m^2+n^2)^5},$$

$$\kappa_{21}(l,m,n) = \frac{M_s}{4\pi}\frac{3ml}{(l^2+m^2+n^2)^5},$$

$$\kappa_{22}(l,m,n) = \frac{M_s}{4\pi}\frac{(2m^2-l^2-n^2)}{(l^2+m^2+n^2)^5},$$

$$\kappa_{23}(l,m,n) = \frac{M_s}{4\pi}\frac{3mn}{(l^2+m^2+n^2)^5},$$

$$\kappa_{31}(l,m,n) = \frac{M_s}{4\pi}\frac{3nl}{(l^2+m^2+n^2)^5},$$

$$\kappa_{32}(l,m,n) = \frac{M_s}{4\pi}\frac{3nm}{(l^2+m^2+n^2)^5},$$

$$\kappa_{33}(l,m,n) = \frac{M_s}{4\pi}\frac{(2n^2-l^2-m^2)}{(l^2+m^2+n^2)^5}. \qquad \text{(Eq. 2.6)}$$

If both of the $\kappa_{pq}(l,m,n)$ and $\vec{M}(i,j,k)$ have the same periods I,J,K with

$$\kappa_{pq}(l,m,n) = \sum_{\lambda=-\infty}^{+\infty}\sum_{\gamma=-\infty}^{+\infty}\sum_{\delta=-\infty}^{+\infty}\kappa_{pq}(l+\lambda I, m+\gamma J, n+\delta K) \qquad \text{(Eq. 2.7)}$$

and $$\vec{M}(i,j,k) = \sum_{\lambda=-\infty}^{+\infty}\sum_{\gamma=-\infty}^{+\infty}\sum_{\delta=-\infty}^{+\infty}\vec{M}(i+\lambda I, j+\gamma J, k+\delta K), \qquad \text{(Eq. 2.8)}$$

$\vec{H}_{de}(i,j,k)$ is called the cyclic convolution and the discrete Fourierm transform of $\vec{H}_{de}(i,j,k)$ can be expressed as

$$\vec{H}_{de}^{D}(i,j,k) = \kappa_{pq}^{D}(l,m,n)\vec{M}^{D}(i,j,k), \qquad \text{(Eq. 2.9)}$$

where $\vec{H}_{de}^{D}(i,j,k)$, $\kappa_{pq}^{D}(l,m,n)$ and $\vec{M}^{D}(i,j,k)$ are the discrete Fourierm transform of $\vec{H}_{de}(i,j,k)$, $\kappa_{pq}(l,m,n)$ and $\vec{M}(i,j,k)$ respectively. Since the original $\kappa_{pq}(l,m,n)$ and $\vec{M}(i,j,k)$ are not periodic, the principle of cyclic convolution can not be applied directly to them. However, cyclic convolution can be used by employing the padding-zero technique as follows:

(1) Add $\kappa_{pq}(I,m,n),\kappa_{pq}(l,J,n),\kappa_{pq}(l,m,K)$ which are zero to the original set of $\kappa_{pq}(l,m,n)$: $l=-I+1,...,-1,0,1,...,I-1$, $m=-J+1,...,-1,0,1,...,J-1$, $n=-K+1,...,-1,0,1,...,K-1$.

(2) Add $\vec{M}(I,j,k)$ to $\vec{M}(2I-1,j,k)$, $\vec{M}(i,J,k)$ to $\vec{M}(i,2J-1,k)$ and $\vec{M}(i,j,K)$ to $\vec{M}(i,j,2K-1)$ which are zero to the original set of $\vec{M}(i,j,k)$: $i=-I+1,...,-1,0,1,...,I-1$, $j=-J+1,...,-1,0,1,...,J-1$, $k=-K+1,...,-1,0,1,...,K-1$.

Then, a cyclic convolution $\vec{H}_{de}(i,j,k)$ with period $2I,2J,2K$ is formed. By using equation 2.9, $\vec{H}_{de}^{D}(i,j,k)$ is obtained. Finally, we carry out inverse Fourierm transform on $\vec{H}_{de}^{D}(i,j,k)$ to obtain the original magnetostatic fields, $\vec{H}_{de}(i,j,k)$.

e. Thermal Stochastic Field $\vec{H}_{st}$:[11,12]

By the fluctuation-dissipation theorem, the thermal stochastic field $\vec{H}_{st}$ has zero mean and is assumed to be Gaussian distribution with a variance σ :

$$\left\langle \vec{H}_{st}^{i}(t) \right\rangle = 0, \qquad \text{(Eq. 2.10)}$$

$$\left\langle \vec{H}_{st}^{\,i}(t)\vec{H}_{st}^{\,j}(t')\right\rangle = \delta_{ij}\delta(t-t')\sigma^2, \qquad \text{(Eq. 2.11)}$$

$$\sigma = \sqrt{\frac{2\alpha k_B T}{\gamma V M_s}}, \qquad \text{(Eq. 2.12)}$$

where δ_{ij} is the Kronecker delta, $\delta(t)$ is the Dirac delta function, indices i and j are the labels of the spins, k_B is the Boltzmann constant, T is the Kelvin temperature, V is the cell volume and α is the damping coefficient.

f. Effective Field $\vec{H}_{eff}$ and Energy.

The effective field $\vec{H}_{eff}$ at spin $\vec{M}$ is the vector addition of the five composite fields:

$$\vec{H}_{eff} = \vec{H}_{ex} + \vec{H}_{an} + \vec{H}_{ze} + \vec{H}_{de} + \vec{H}_{st}. \qquad \text{(Eq. 2.13)}$$

The energy of spin $\vec{M}$ is also the addition of the five composite energies:

$$E_{sp} = E_{ex} + E_{an} + E_{ze} + E_{de} + E_{st},$$

$$E_{ex} = -\mu_0 \vec{H}_{ex} \bullet \vec{M}$$

$$E_{an} = -\mu_0 \vec{H}_{an} \bullet \vec{M}$$

$$E_{ze} = -\mu_0 \vec{H}_{ze} \bullet \vec{M}$$

$$E_{de} = -0.5\mu_0 \vec{H}_{de} \bullet \vec{M}$$

$$E_{st} = -\mu_0 \vec{H}_{st} \bullet \vec{M}. \qquad \text{(Eq. 2.14)}$$

The total energy of the material is the sum of the energy at each spin.

3. Integration of LLG Ordinary Differential Equations (ODE):

The LLG equation is an initial-value ODE and is solved numerically. At time t, the effective field, $\vec{H}_{eff}$, at each spin $\vec{M}$ is calculated as discussed above. $\Delta\vec{M}$ is obtained by integration the LLG equation with a small time stepsize, Δt. Since the magnitude of the $\vec{M}$ is assumed to be constant, the new $\vec{M}$ is obtained by normalizing the vector addition of the old $\vec{M}$ and $\Delta\vec{M}$. In most cases, the LLG equation is stiff, which means that Δt must be chosen carefully to keep the integration stable and efficient. Many advanced algorithms with adaptive stepsize control have been developed to achieve some predetermined accuracy in the solution with minimum computational effort. Such methods include the backward Euler, implicit Adams-Moulton and embedded Runge-Kutta method. In our calculations, the criteria for the equilibrium state is that the maximum of the magnitude of the reduced torque $|\vec{M}\times\vec{H}_{eff}|$ is less than 1.0×10^{-5}. When the equilibrium state is approached, Δt must be decreased to minimize the torque. Therefore, a variable-order ODE solver was used to solve the LLG equation. The three methods with different order of convergence used in this work are first-order Euler method, second-order predictor-corrector Adams-Moulton method and fifth-order embedded Runge-Kutta method. The calculations of the three methods are as follows:

a. First-Order Euler Method:[32]

$$\vec{M}(t+\Delta t)=\vec{M}(t)+\vec{F}(t)\Delta t, \qquad \text{(Eq. 2.15)}$$

$$\Delta = 0.5\left|\vec{F}(t+\Delta t) - \vec{F}(t)\right|\Delta t \qquad \text{(Eq. 2.16)}$$

b. Second-Order Predictor-Corrector Adams-Moulton Method:[32]

$$\vec{M}^{P}(t+\Delta t) = \vec{M}(t) + \vec{F}(t)\Delta t\,, \qquad \text{(Eq. 2.17)}$$

$$\vec{M}(t+\Delta t) = \vec{M}(t) + \frac{1}{2}(\vec{F}(t) + \vec{F}^{p}(t+\Delta t))\Delta t\,, \qquad \text{(Eq. 2.18)}$$

$$\Delta = \left|\vec{M}(t+\Delta t) - \vec{M}^{P}(t+\Delta t)\right| \qquad \text{(Eq. 2.19)}$$

c. Fifth-Order Embedded Runge-Kutta Method:[32]

$$\vec{k}_1 = \vec{F}(M)\Delta t\,, \qquad \text{(Eq. 2.20)}$$

$$\vec{k}_2 = \vec{F}(\vec{M} + \frac{1}{5}\vec{k}_1)\Delta t\,, \qquad \text{(Eq. 2.21)}$$

$$\vec{k}_3 = F(\vec{M} + \frac{3}{40}\vec{k}_1 + \frac{9}{40}\vec{k}_2)\Delta t\,, \qquad \text{(Eq. 2.22)}$$

$$\vec{k}_4 = F(\vec{M} + \frac{3}{10}\vec{k}_1 - \frac{9}{10}\vec{k}_2 + \frac{6}{5}\vec{k}_3)\Delta t\,, \qquad \text{(Eq. 2.23)}$$

$$\vec{k}_5 = F(\vec{M} - \frac{11}{54}\vec{k}_1 + \frac{5}{2}\vec{k}_2 - \frac{70}{27}\vec{k}_3 + \frac{35}{27}\vec{k}_4)\Delta t\,, \qquad \text{(Eq. 2.24)}$$

$$\vec{k}_6 = F(\vec{M} + \frac{1631}{55296}\vec{k}_1 + \frac{175}{512}\vec{k}_2 + \frac{575}{13824}\vec{k}_3 + \frac{44275}{110592}\vec{k}_4 + \frac{253}{4096}\vec{k}_5)\Delta t \qquad \text{(Eq. 2.25)}$$

$$\vec{M}(t+\Delta t) = \vec{M}(t) + \frac{37}{378}\vec{k}_1 + 0\vec{k}_2 + \frac{250}{621}\vec{k}_3 + \frac{125}{594}\vec{k}_4 + 0\vec{k}_5 + \frac{512}{1771}\vec{k}_6 \qquad \text{(Eq. 2.26)}$$

and

$$\Delta = (\frac{37}{378} - \frac{2825}{27648})\left|\vec{k}_1\right| + (0-0)\left|\vec{k}_2\right| + (\frac{250}{621} - \frac{18575}{48384})\left|\vec{k}_3\right| + (\frac{125}{594} - \frac{13525}{55296})\left|\vec{k}_4\right| + (0 - \frac{277}{14336})\left|\vec{k}_5\right| + (\frac{512}{1771} - \frac{1}{4})\left|\vec{k}_6\right| \quad \text{(Eq. 2.27)}$$

where Δ is the local error estimation of stepsize Δt. The maximum Δ allowed in each step is 1.0×10^{-4} which is approximately 0.01 degree. The selection of which of the three methods is used is shown as the following procedure diagram:

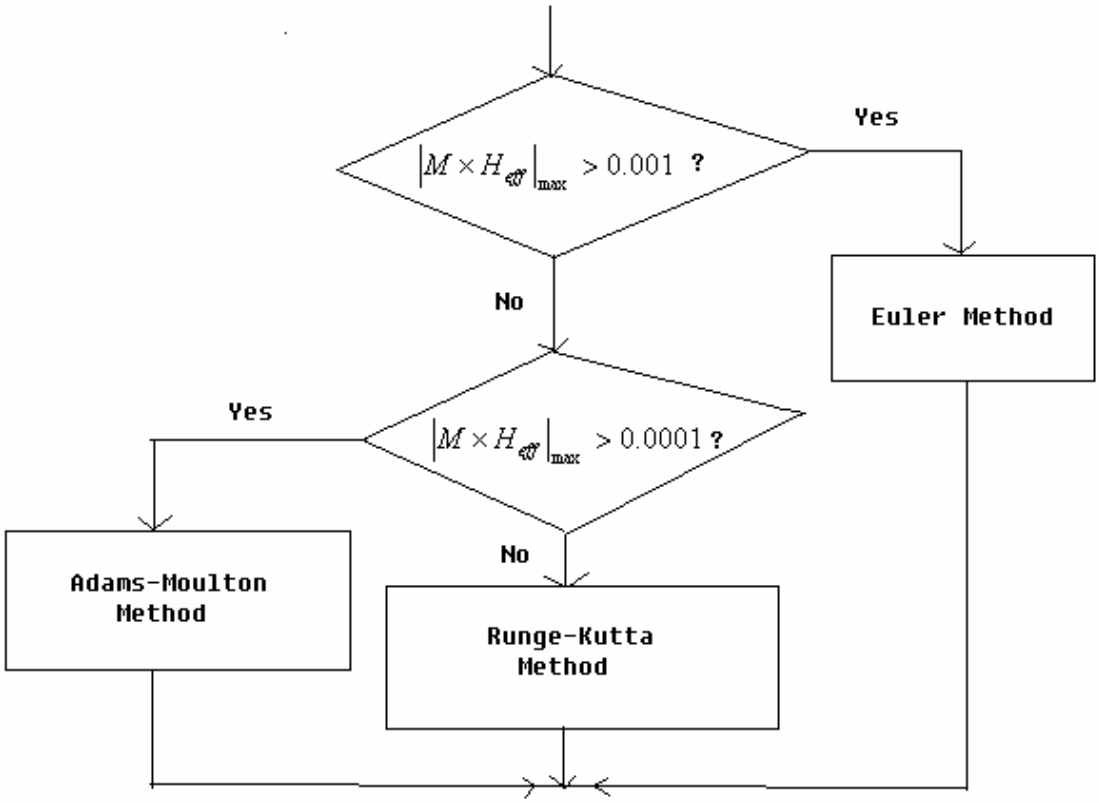

FIG. 2.1. Procedure diagram for ODE solver method selection

CHAPTER THREE:

"SEED" INDUCED MAGNETISM REVERSAL

1. Material Properties and Modeling of Cobalt Element Array and "Seed":

There were two segments used in the calculations presented in this chapter, one is a cobalt element array and the other is the induction pillar or "seed". Both were modeled as boxes of cubic cells with exchange constant $A = 1.4 \times 10^{-11} J/m$, uniaxial anisotropy $K_1 = 5.0 \times 10^5 J/m^3$ and saturation magnetization $M_s = 1.4 \times 10^6 A/m$.[10] These parameters are consistent with cobalt. Since the exchange length of cobalt is $\sqrt{\frac{2A}{\mu_0 M_s^2}} \approx 3.37nm$, the cell sizes of $2.5nm$ and $1.25nm$ were used to avoid a underestimation of the exchange effect. Both of the cell sizes produced similar results. Thus, all of the computations presented in this chapter were done with the cell size of $2.5nm$ to save computation time. We assume that all of the cells had the same easy axis direction, along the long axis of the element array. The element array and "seed" had the same cutting area, but with different lengths along the easy axis. The dimension of the "seed" was $10nm \times 5nm \times 5nm$ $(4cell \times 2cell \times 2cell)$ and the element array was $50nm \times 5nm \times 5nm$ $(20cell \times 2cell \times 2cell)$.

Initially, all of the spins in both the element array and the seed remained aligned along the easy axis but with different directions even after releasing the external field

applied along the easy axis, as shown in Fig. 3.1 and Fig 3.2. The spins remained aligned even with the thermal fluctuation at room temperature because of the strong anisotropy interactions in bulk cobalt. Cobalt is a magnetically hard material.

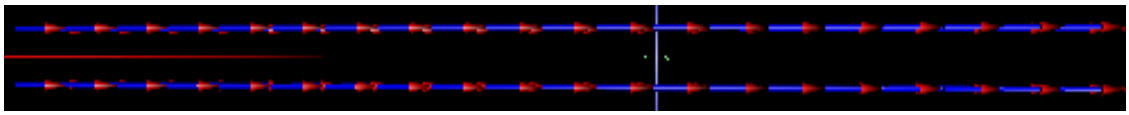

FIG. 3.1 Element array

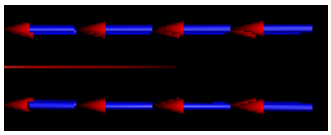

FIG. 3.2 Induction pillar (“seed”)

2. Magnetic Reversal without “Seed”:

We applied external magnetic fields with different amplitude along the easy axis to the initially saturated element array without using the “seed”. If the magnitude was less than $0.7 Tesla$, the spins in element array did not flip since the applied field was not strong enough to overcome the energy barrier produced by the combined effects of exchange and anisotropy fields. If the magnitude of applied field is greater than $0.7 Tesla$, the flipping took place at either end of the element array because there was few exchange interaction on the ending spins to keep them along the easy axis. We

traced the spins during the reversal and showed the snapshots in Fig. 3.3. Also, due to the exchange interaction, all of the spins rotated away from the easy axis and are ready to flip as shown in Fig. 3.3.2. Thus, the next flipping could take place on any part of the element array. Even though there may be some discrete flipping parts, the spins in the same flipping part moved coherently as shown in Fig. 3.3.2 to Fig. 3.3.9. Although the total flipping time depended on the magnitude of the applied field, the switching usually took less than $0.01ns$. Thus, the magnetic reversal without the "seed" followed the coherent mechanism. In such reversal, there was no domain wall observed and the spins did not flip consecutively.

3. Incoherent Magnetic Reversal Induced by "Seed":

From the discussion of Part 2, we know that incoherent switching and domain wall could not be induced in the element array simply by applying an external magnetic field along the easy axis. However, by placing a "seed" segment with antiparallel spins adjacent to the element array, a domain wall could be introduced. By applying an external magnetic field with specific magnitude, the domain wall could be driven to propagate along the easy axis and the spins can switch consecutively.

We moved the "seed" next to the element array, as shown on Fig. 3.4.1, and applied an external field along the easy axis. The magnitude of the field was $0.667Tesla$, which is close to the anisotropy field of the cobalt element array, $H_{an} = \frac{2K_1}{\mu_0 M_s}$. The reversal of spins in the element array was traced and snapshots at different times are shown in Fig. 3.4.

H_{app}

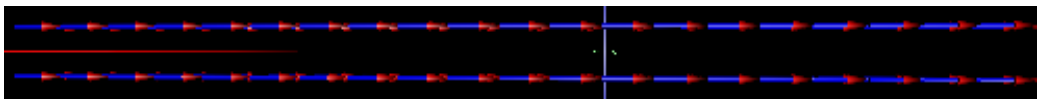

(1) $t = 0s$

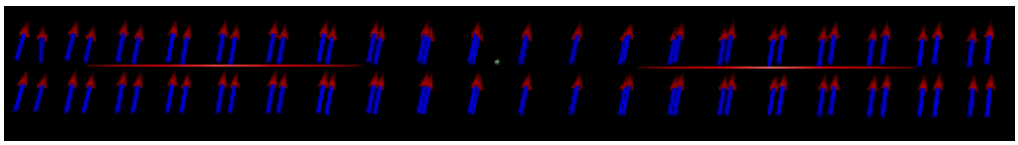

(2) $t = 1.0 \times 10^{-12} s$

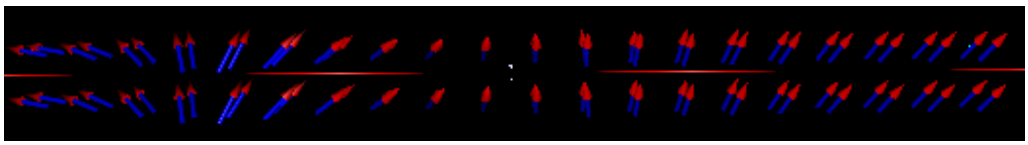

(3) $t = 2.0 \times 10^{-12} s$

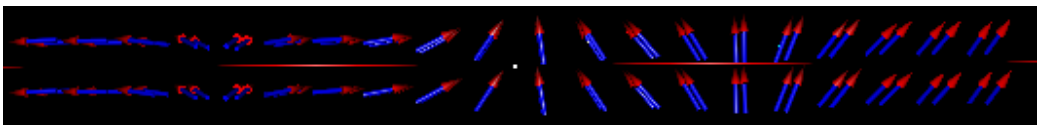

(4) $t = 3.0 \times 10^{-12} s$

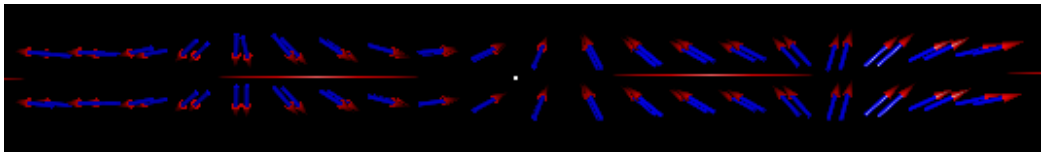

(5) $t = 4.0 \times 10^{-12}\, s$

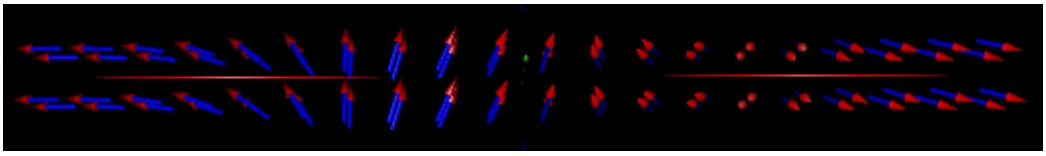

(6) $t = 5.0 \times 10^{-12}\, s$

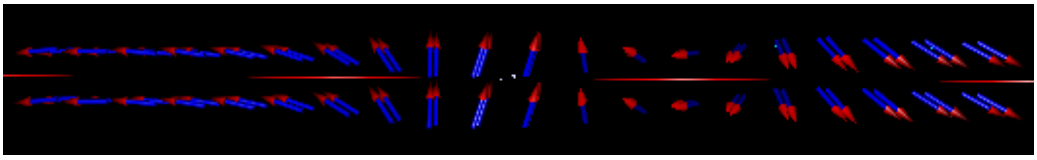

(7) $t = 6.0 \times 10^{-12}\, s$

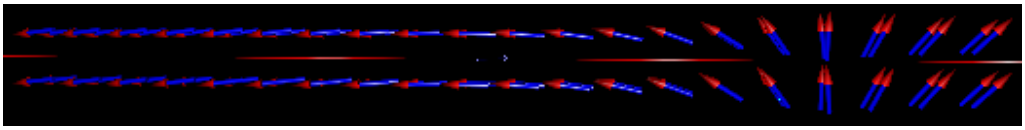

(8) $t = 7.0 \times 10^{-12}\, s$

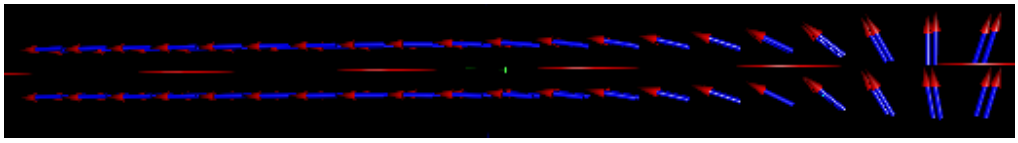

(9) $t = 8.0 \times 10^{-12}\, s$

FIG. 3.3 Snapshots of spins at element array under $H_{app} = 1.0 Tesla$ without "seed"

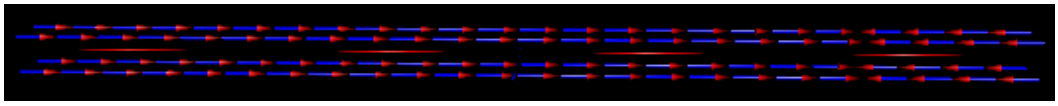

(1) $t = 0s$

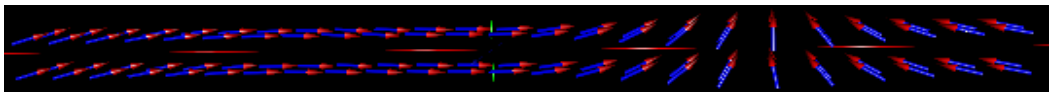

(2) $t = 1.0 \times 10^{-10} s$

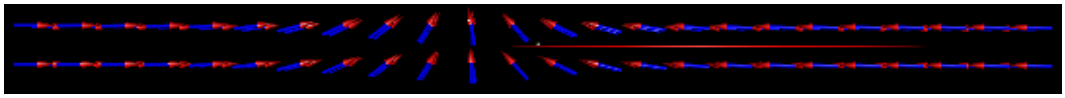

(3) $t = 5.5 \times 10^{-10} s$

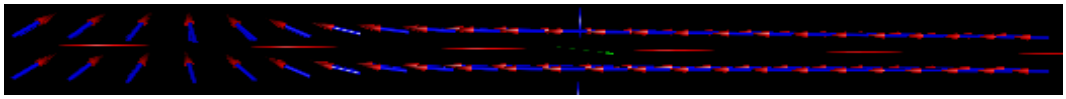

(4) $t = 9.0 \times 10^{-10} s$

FIG. 3.4 Snapshots of spins at element array under $H_{app} = 0.667 Tesla$ with “seed”

Due to the strong exchange and magnetostatic interactions, the energy barrier of the element adjacent to the seed element is lowered dramatically. By applying an external field of magnitudes of $0.667 Tesla$, the effects of the anisotropy interactions are cancelled. Thus, the spins switched incoherently and sequentially along the easy axis during the reversal. A domain wall approximately $20nm$ ($8cells$) wide was formed and moved rotationally along the easy axis. This spin reversal mechanism has been reported.[6]

4. Propagation of the Domain Wall:

The spins in the plane perpendicular to the easy axis rotated coherently due to the strong exchange interaction between neighboring spins. The lag time between switching of neighboring spins is short, usually less than $10^{-12} s$. Therefore, we can divide the array into "pillars", each pillar consisting of four cells. Thus, there are 20 pillars in our system. The first passage time of each pillar was the average time of the four spins in that part when they crossed the plane perpendicular to the easy axis. Because of the strong interactions of both anisotropy and applied field, the energy barrier to reverse the spin flip was quite large. Therefore, the first passage time was the switching time.

We traced the reversal of the spins in the element array and recorded the first-passage time of each pillar. The thermal effect was studied at three temperatures $200K$, $250K$ and $300K$. For each temperature, 200 calculations were performed and a statistical analysis carried out.

The switching times of the pillars under $Happ = -0.6700 Tesla$ at $T = 200k$, $T = 250k$ and $T = 300k$ are shown in Fig 3.6, Fig 3.7 and Fig 3.8.

From Fig 3.6, Fig 3.7 and Fig 3.8, the calculations performed at the three temperatures obtained similar results. Because of the large anisotropy constant of bulk cobalt, thermal fluctuation had only a small effect on the induced magnetic reversal even at room temperature. Note that the error bars on the switching time for each of the middle sixteen pillars do not overlap. Thus each pillar can be considered to switch consecutively.

5. Stability of the Domain Wall:

The stability of the domain wall at room temperature was studied by tracing the spins after exposing the element array to an applied field for time $t_n + \frac{t_{n+1} - t_n}{2}$, where t_n is the switching time for part n, then releasing the applied field. The snapshots of the spins after releasing the applied field are shown in Fig. 3.5.

We found that the domain wall was relatively stable and its position in the element array did not move even in the presence of thermal fluctuations at room temperature because the energy barrier of the movement of the domain wall is the sum of the energy barrier that should be overcome by each pillar in the domain wall. The long term thermal stability of our system is estimated to be better than single domain bit dots because of the higher energy barrier.

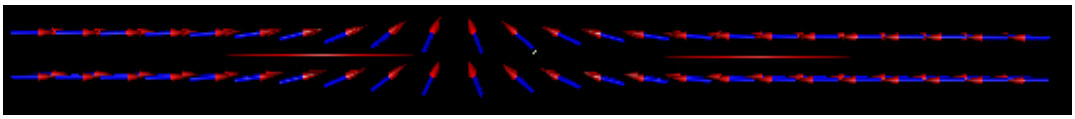

$t = 10.0ns$

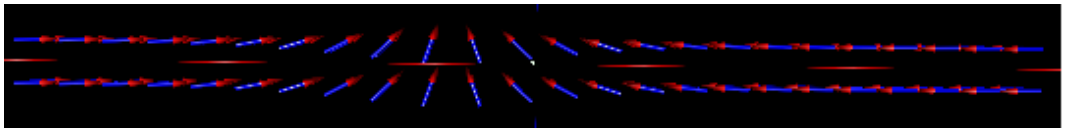

$t = 100.0ns$

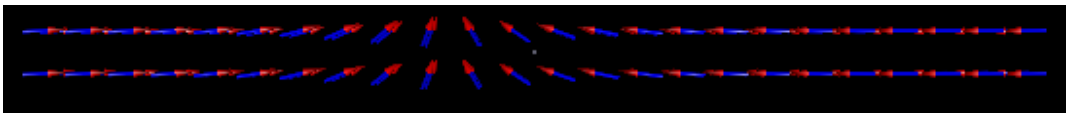

$t = 1000.0ns$

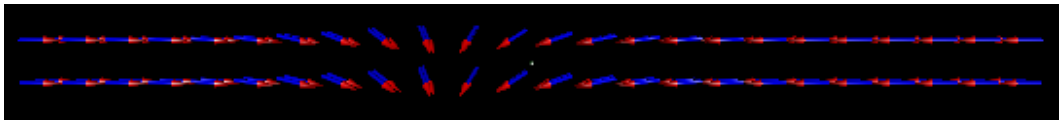

$t = 10000.0ns$

FIG 3.5 Snapshots of element array after releasing external applied field for time t

6. The Relaxed Magnetization after Releasing of Applied Field:

Since the first passage times of the 16 middle pillars in the element array were known and were nearly linear in the index of the pillar, and since the domain wall was stable after releasing the applied field, the number of pillars to be switched can be controlled by exposing the element array to an applied field for a specific time. The total magnetization of the element array and the seed (more conveniently measured than the magnetization of only the element array), after exposure for time $t_n + \frac{t_{n+1} - t_n}{2}$, then relaxed for $1.0 \times 10^{-5} s$ is shown in Fig 3.9. The deviation in the reduced magnetization due to the thermal fluctuation is only ± 0.002. From Fig 3.9, we can see that the relative magnetization can be approximated by the "net" unswitched pillars which is the difference between numbers of the switched pillars $(4 + i)$ and the unswitched pillars $(20 - i)$, divided by the number of total pillars (24), where i is the number of switched pillars in the element array.

Thus, the number of switched pillars can be controlled by the application of an external magnetic field for a specific duration time and accurately measured by measuring the magnetization of the element array.

7. Usage as Information Storage Medium:

In this system, the element array acts as a 4-bit $(2^4 = 16)$ ultra-fast storage medium. From Fig. 3.8, we see that the total switching time to switch all 16 pillars is

less than $1ns$ at room temperature, thus, the maximum write time is $1ns$. For one byte $(1Byte = 8Bits)$ of information, it took 2 nanoseconds, which is significantly faster than the current industry standard. The information can be retrieved by reading the magnetization of the whole element array. Thus, this method of information storage overcomes the limitation of current ultra-high density storage schemes which are limited by the necessarily small size of the read head where individual bits are read. Since the information is stored in hex $(2^4 = 16)$ format, rather than the binary $(2^1 = 2)$ format, the operation times to locate and move the magnetic head can be decreased dramatically. For example, to write 4 bits of information in a traditional storage medium, it costs four head operations. But for the pillar array, only one operation is needed. These factors suggest a way to overcome the bottleneck of the speed of ultra-fast media storage where the time for head operations dominates the physical write time of the media. The information storage density of the element array is quite high. In this system, 8 bits of information are stored in an array of $50nm$ by $10nm$ yielding an areal storage density of roughly $10^4 GigaBits/cm^2$, while this appears to exceed the superpara magnetic limit it does not since the magnetic volume is the volume of the entire array which is thermally stable. Although the large uniaxial anisotropy constant K_1 of cobalt increases the magnitude of the applied magnetic field that propagates the domain wall, it is necessary for the thermal stability of the domain wall after the applied field is released.

8. Conclusions:

We have described how a "seed" induced domain wall in a magnetic element array can be used to produce a novel, fast, ultra-high density storage medium. A $4-bit$ storage medium with write time of 1 ns and areal storage densities of roughly $10^4 GigaBits/cm^2$ which are stable at room temperature is feasible. Since the magnetization of the entire array is used to store the information, the read head size would be $50nm$ which is significantly larger than that proposed for conventional ultra-high storage media. The disadvantage of the proposed scheme is that the data is stored in hex $(2^4 = 16)$ format which limits the size of the digital number stored in the array. Another possible application of the induced pillar is as a computation register. In this device, the operation of addition and minus can be obtained by moving the domain wall freely along the easy axis.

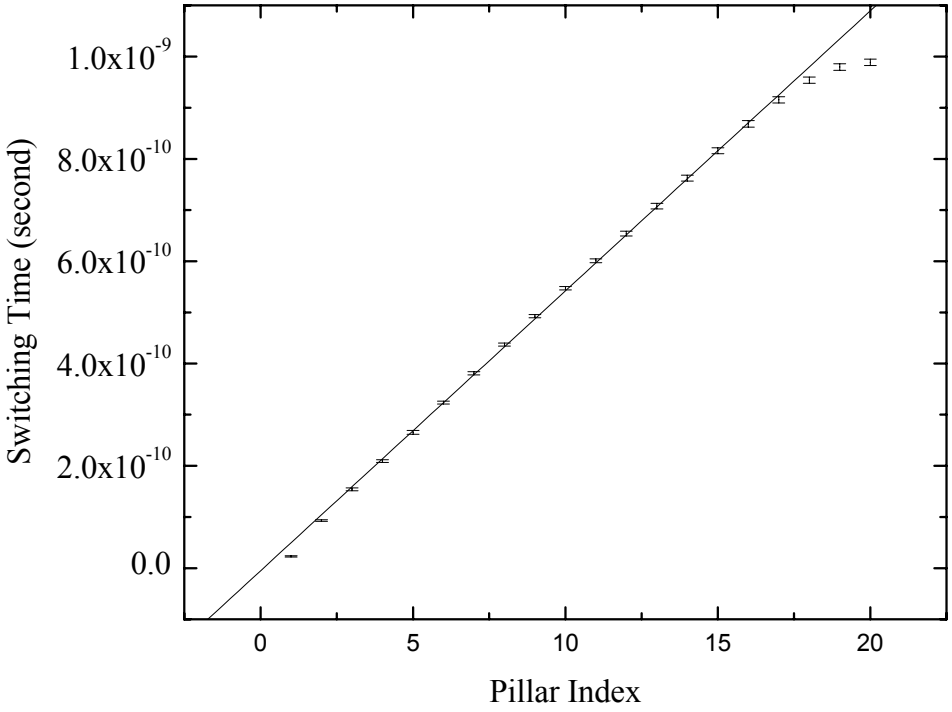

Fig 3.6 The switching time as function of part index at $200K$,

The equation of the straight line fitting for the 16 middle parts is

$$Y = -5.02 \times 10^{-12} + 5.47 \times 10^{-11} X ,$$

the error bars denote ± standard deviation by 95%

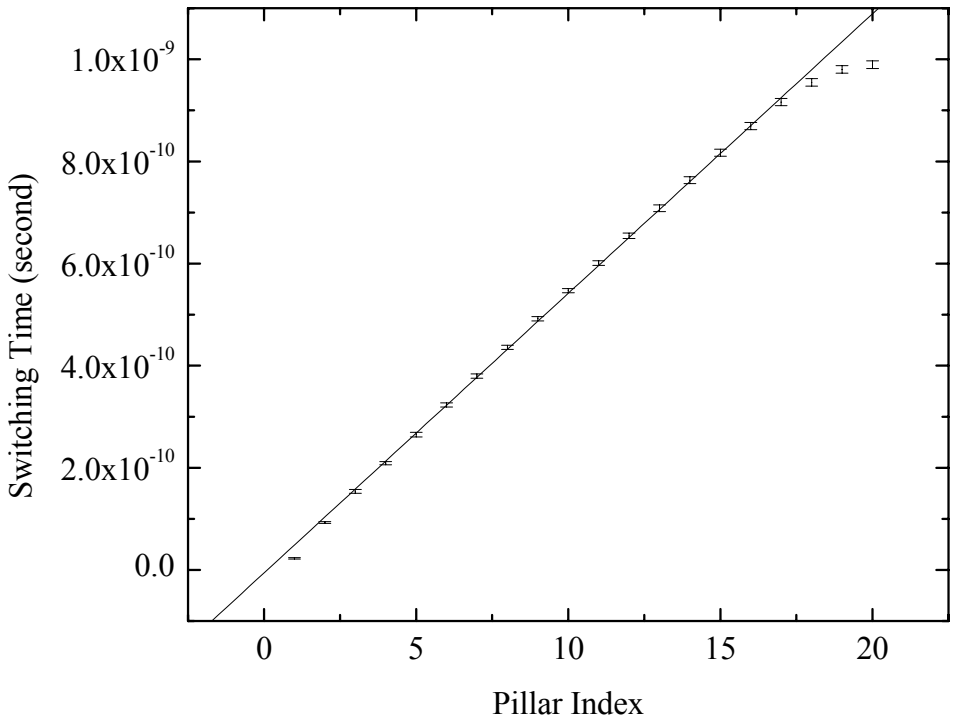

Fig 3.7 The switching time as function of part index at $250K$,

The equation of the straight line fitting for the 16 middle parts is

$$Y = -5.83 \times 10^{-12} + 5.47 \times 10^{-11} X ,$$

the error bars denote ± standard deviation by 95%

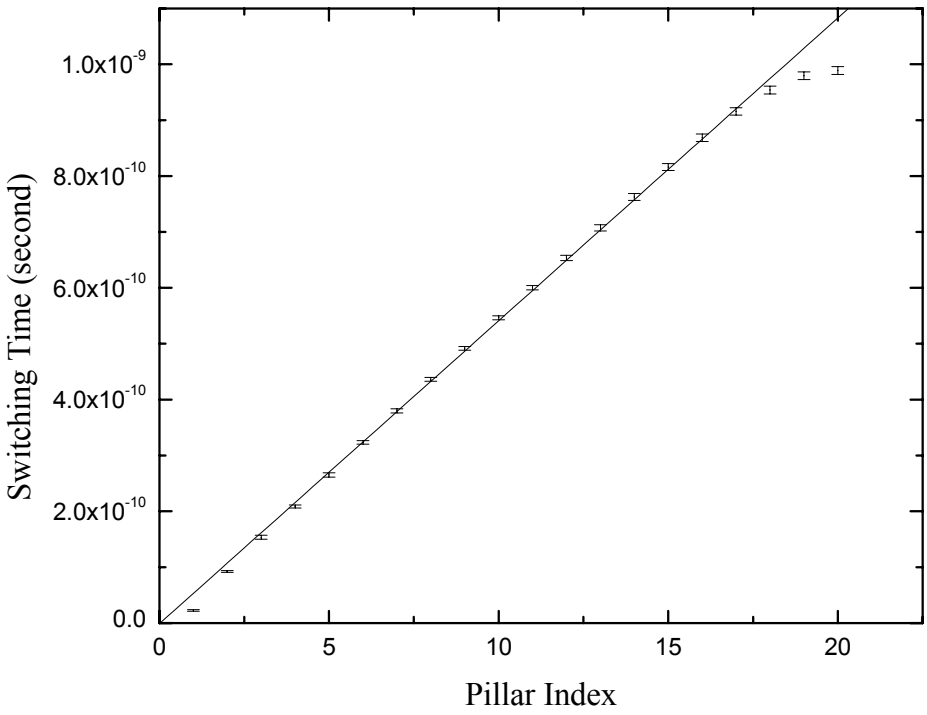

Fig 3.8 The switching time as function of part index at $300K$,

The equation of the straight line fitting for the 16 middle parts is

$$Y = -1.045 \times 10^{-12} + 5.42 \times 10^{-11} X ,$$

the error bars denote ± standard deviation by 95%

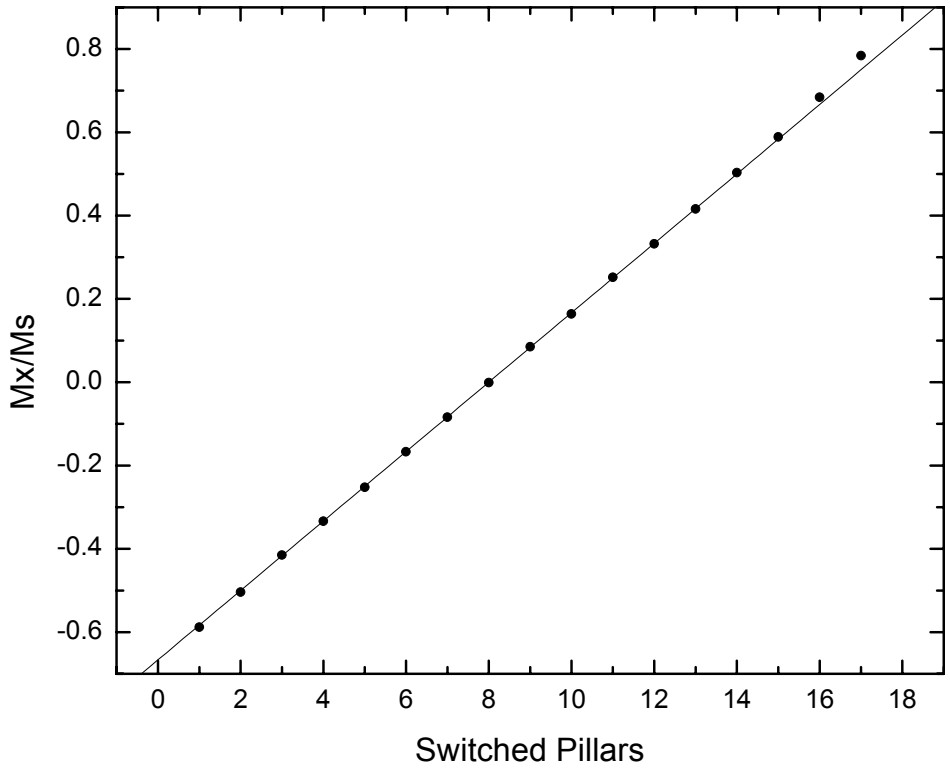

FIG. 3.9 Relative magnetization along easy axis as function of switched pillars

CHAPTER FOUR: EFFECTS OF APPLIED FIELDS, CELLSIZE AND CUTTING AREA

In Chapter Three, a novel method to store information by the position of the domain wall in an element array rather than in the magnetic domains was proposed to overcome the superparamagnetic limitation to ultra-high density storage. Since the evolution of the spins can be varied according to amplitude of the external fields, cellsize chosen in the calculations and the cutting area of the element array and seed, the effects of them on the propagation of the domain wall were examined to study the reversal mechanism and to minimize the effect of the thermal fluctuation on the switching time. A sinusoidal applied field with specific period was used to simulate digital like signal to generate a single switching event.

1. Effect of Applied Field Magnitude:

An external magnetic field was applied along the easy axis of an element array with cellsize $2.5nm$ and dimension $50nm \times 5nm \times 5nm$ $(20cell \times 2cell \times 2cell)$. Field amplitudes less than $0.25Tesla$ are not able to overcome the energy barrier needed to propagate the domain wall. For field amplitudes greater than $1.50Tesla$, magnetic reversal occurred randomly both spatially and temporally in the element array and the spins did not switch consecutively along the easy axis. In the field amplitudes range

between $0.25Tesla$ to $1.50Tesla$, a domain wall was observed to propagate along the easy axis. We traced the reversal of the pillars in the element array and recorded the first-passage time of each pillar. One hundred simulation runs were performed for each of four applied fields and a statistical analysis carried out (Fig. 4.1). The propagation of the domain wall depended on the magnitude of the applied field. The reversal time for the entire element array can vary from $1.40ns$ for the lowest field $0.50Tesla$, to $0.50ns$ for the highest field, $1.10Tesla$.

The effect of thermal fluctuations on the switching time is indicated by the error bars in Fig.4.1. Thermal noise manifests itself as a variance in the switching time of an individual pillar. This variance gives rise to the error bars in Fig. 4.1. We can define a signal-to-noise ratio, SNR, as the ratio of the average height of the error bars to the average switching times between the neighboring pillars. We have determined the SNR at eleven fields with magnitudes from $0.30Tesla$ to $1.30Tesla$ (Fig. 4.2). The thermal fluctuation had minimum effect at applied magnitudes of $0.70Tesla$ and $0.80Tesla$. At larger or smaller fields the SNR decreases. Thus only fields with magnitudes from $0.60Tesla$ to $1.10Tesla$ have an SNR>2 and can be practically applied.

2. Mechanism of Magnetic Reversal:

Because the SNR is an indication of the effect of the thermal flutuations on the local magnetic field, the different SNRs suggest different magnetic reversal mechanisms. To study the magnetic reversal mechanism, we scanned the energy of a spin and the angle θ between the spin and the easy axis as a function of time at three

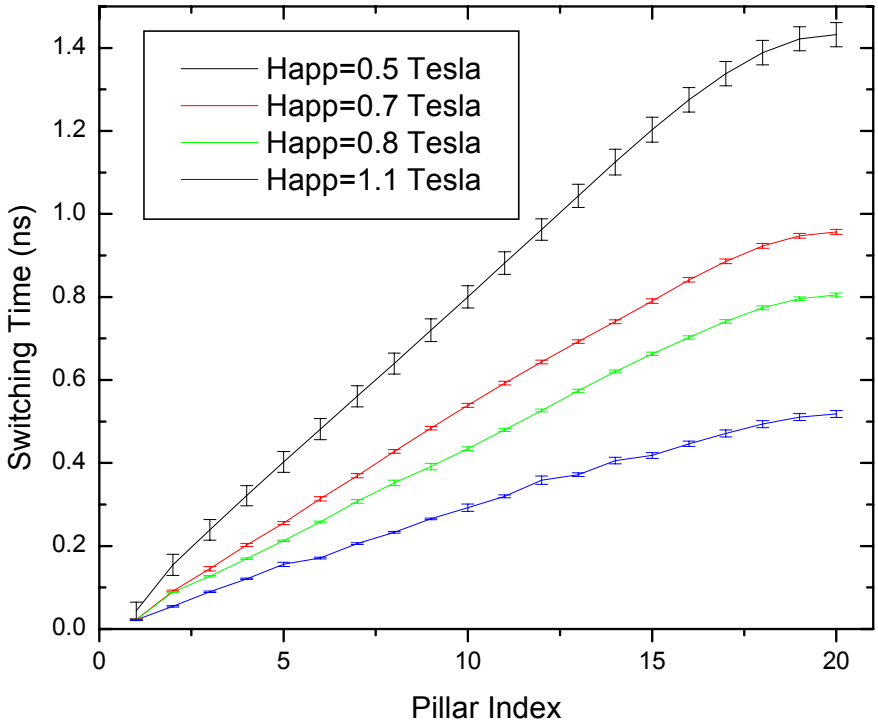

FIG. 4.1 Propagation of the domain wall at different applied field magnitudes

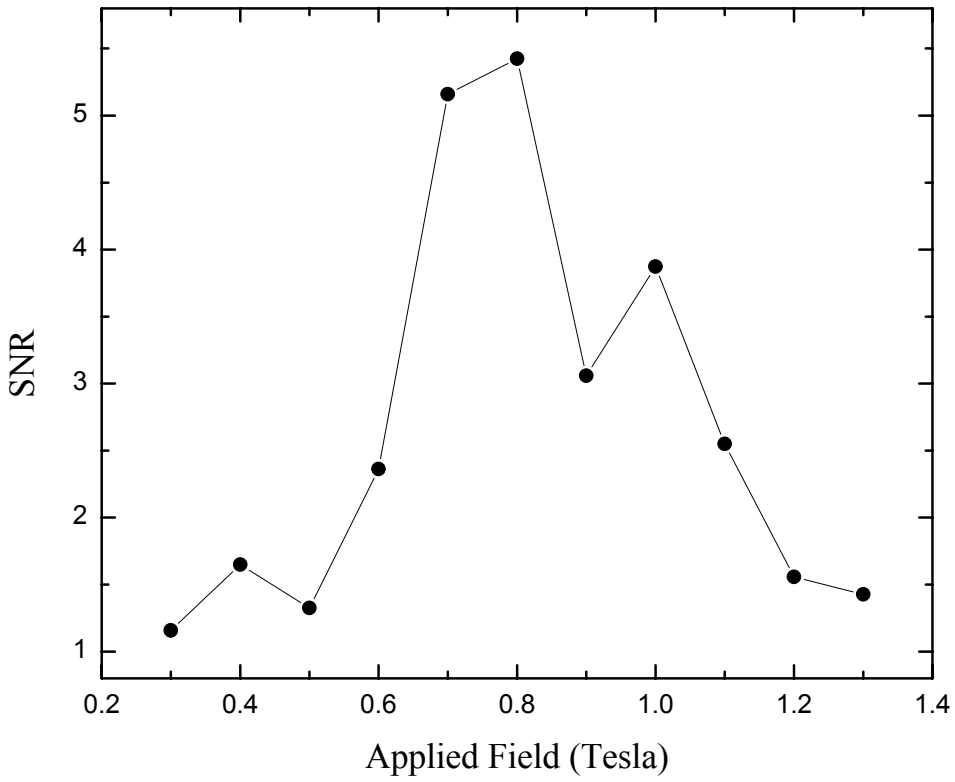

FIG. 4.2 SNR as a function of applied field magnitude

different fields, $0.4Tesla$, $0.7Tesla$ and $1.4Tesla$ (Fig. 4.3). The spin monitored was chosen to be the $10th$ pillar of the 20-pillar element array. The "•"s in Fig. 4.3 indicate the switching time of the pillars.

The labels A, B, C, D and E denote the pillars prior to the pillar being monitored. Fig. 4.3. indicates that the energy and angle of the spin do not change significantly at the previous pillar switch until the switching of the pillar three pillars away. From this, we can estimate the half effect length of the propagation domain wall to be $7.5nm$ $(3cells)$. With this information, we seek to understand why the SNR decreases at low and high applied fields.

If the magnitude of the applied field is low (Fig. 4.3.1), the energy increases as the spin rotates from one orientation or spin state to the next. This increase is mainly due to the exchange interactions as can be seen in Fig. 4.4. The exchange interaction does not have a preferred orientation relative to the pillar array. Therefore, the thermal fluctuation field which is orientational random, may sometimes accelerate and sometimes retard the propagation of the domain wall. Thus, the variance in the switching time and, therefore the SNR, is decreased at low applied field.

When an intermediate field is applied, (Fig. 4.3.2), there are two metastable points on the energy profile as the spin rotates from state A to state B or state B to state C. As the domain wall propagates, the spins in each pillar climb up the energy barrier driven by the applied field, they relax into a metastable state and then climb up the next energy barrier. This process continues until the spin switches. At intermediate field strengths, metastable states exist during the propagation of the domain wall. The thermal noise is negligible at intermediate fields and a good linear relationship between

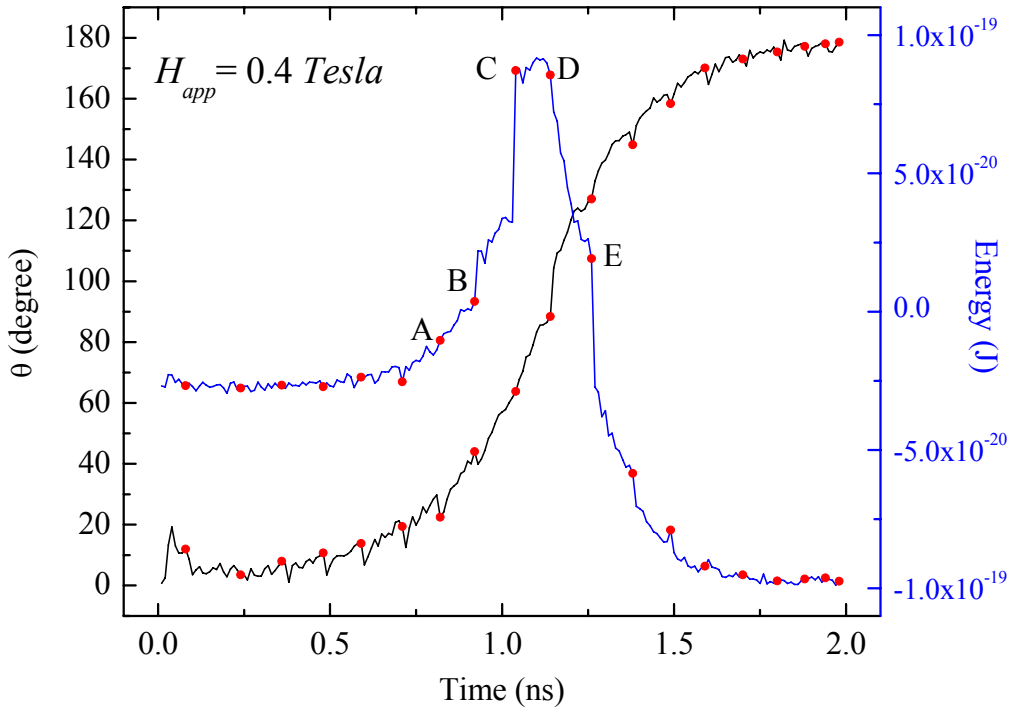
H_{app} = 0.4 *Tesla*
A
B
C
D
E
θ (degree)
Energy (J)
Time (ns)
180
160
140
120
100
80
60
40
20
0
0.0
0.5
1.0
1.5
2.0
1.0x10^{-19}
5.0x10^{-20}
0.0
-5.0x10^{-20}
-1.0x10^{-19}

(1)

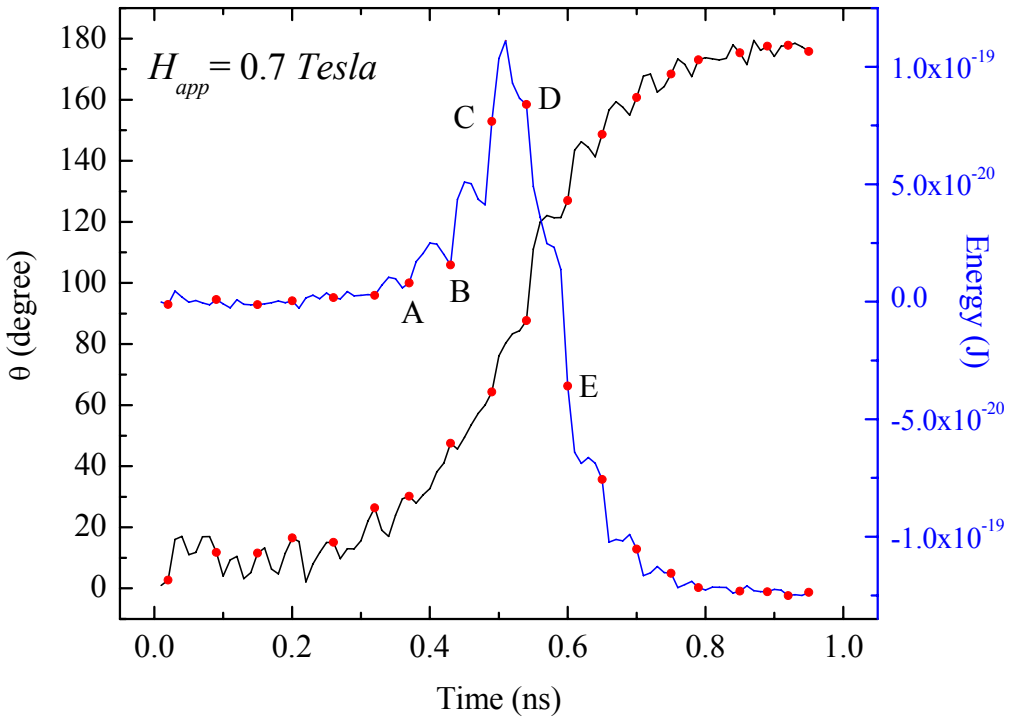
H_{app} = 0.7 *Tesla*
A
B
C
D
E
θ (degree)
Time (ns)
Energy (J)
180
160
140
120
100
80
60
40
20
0
0.0
0.2
0.4
0.6
0.8
1.0
1.0x10-19
5.0x10-20
0.0
-5.0x10-20
-1.0x10-19

(2)

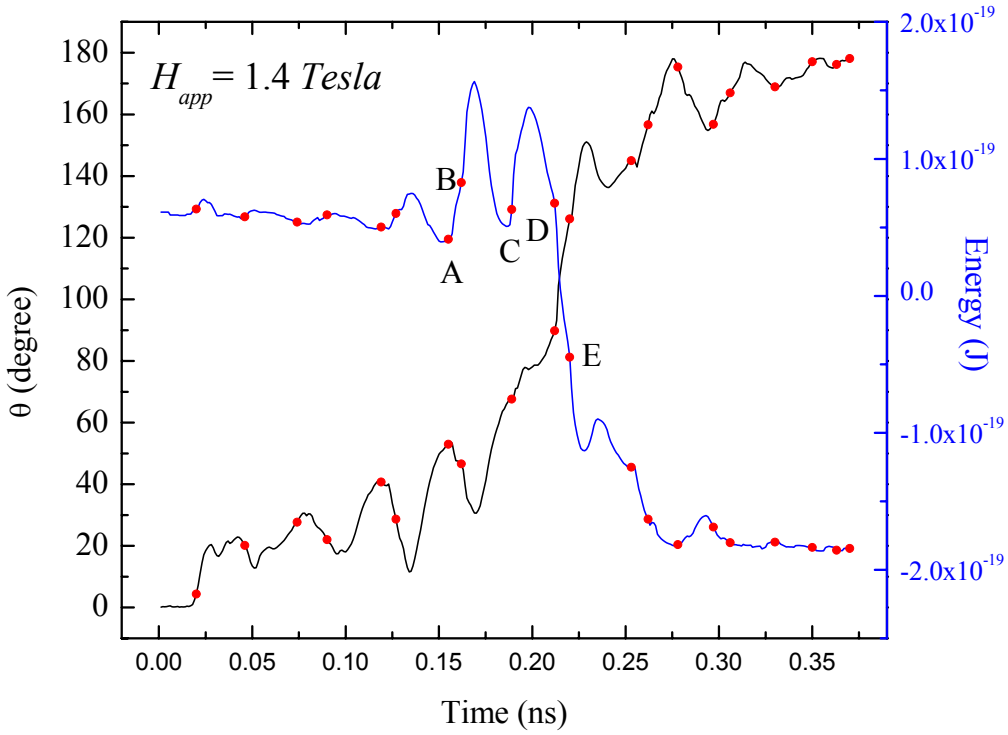

(3)

FIG. 4.3 Energy and θ Profile with different applied field magnitudes

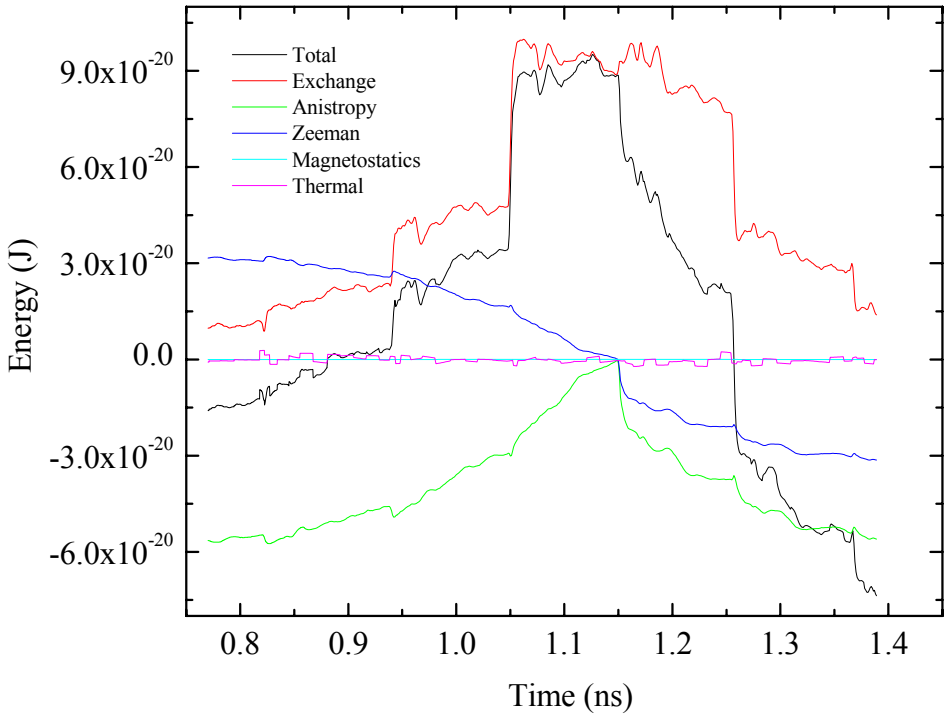

FIG. 4.4 High resolution energy profile at $H_{app} = 0.4 Tesla$

the switching time and the pillar index is found as shown in Fig 4.1.

At large applied fields (Fig. 4.3.3), spins not adjacent to the domain wall begin to sample orientations with relatively large deviation relative to the easy axis direction. When the sum of the applied field and the thermal fluctuation field exceeds the anisotropy field for pillars adjacent to the domain wall, then these pillars flip. This gives rise to decreased SNR at high applied fields.

3. Effect of Cutting Area:

From Eq.2.12, we see that the thermal fluctuation can be reduced by increasing the cell volume, V. Since the spins within a pillar rotate coherently, it seems possible to reduce the thermal effect by increasing the cutting area of the element array. Before studying the effect of the cutting area on the domain wall propagation, we examine the coherence of the switching of the spins. We define T_1 as the switching time difference between the switchings of the first and last spins within a pillar, and T_2 as the switching time difference between the last switched spin and the first switched spin in adjacent pillar. The incoherence of the rotation can be indicated by the incoherence coefficient $\sum_i^n T_{i1} \Big/ \sum_i^n T_{i2}$ where T_{i1} and T_{i2} are the T_1 and T_2 at pillar i respectively, and n is the number of pillars. The incoherence coefficient for different areas under applied field $0.7 Tesla$ is shown in Fig. 4.5. When the cutting area increases, the effect of the exchange interactions between the spins in the same pillar become weaker. A large

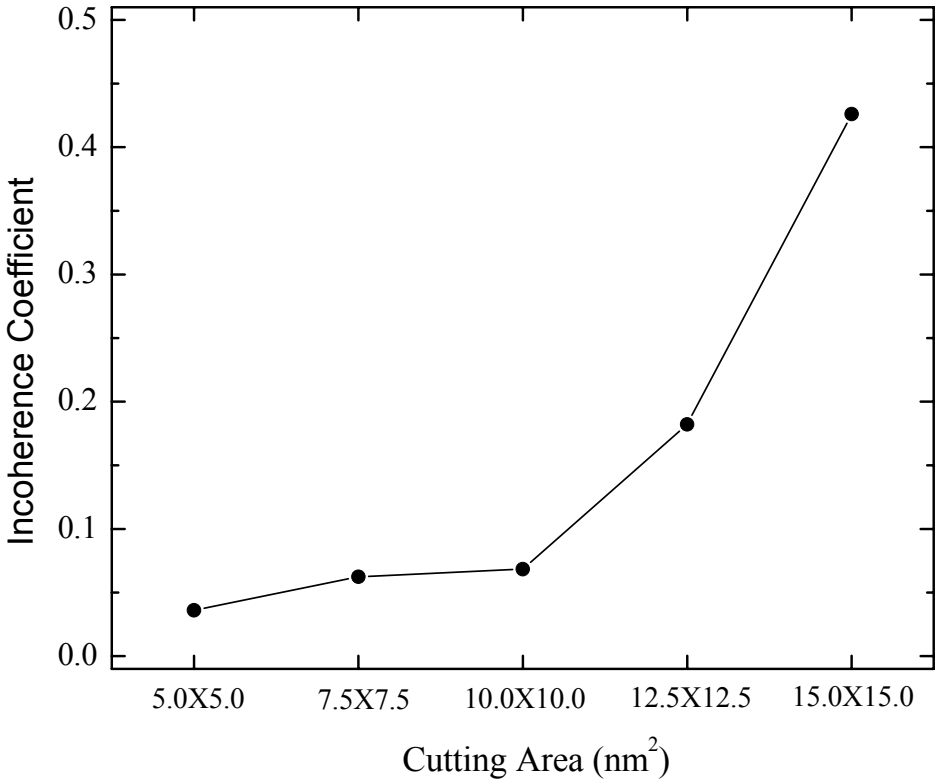

FIG. 4.5 Rotation incoherence coefficient with different cutting area

exchange interaction is needed for coherent rotation. Thus, the incoherence coefficient increases with increasing cutting area as shown in Fig. 4.5. The incoherence coefficient increases dramatically when the cutting area is above $10.0nm \times 10.0nm$ $(4cells \times 4cells)$, the assumption of the coherent rotation is strictly valid only when the cutting area is less than $10.0nm \times 10.0nm$ $(4cells \times 4cells)$.

The switching time with the indicated variance is shown in Fig. 4.6. For several cutting areas, $5.0nm \times 5.0nm$ $(2cells \times 2cells)$, $7.5nm \times 7.5nm$ $(3cells \times 3cells)$ and $10.0nm \times 10.0nm$ $(4cells \times 4cells)$, the cutting area does not have a significant effect on the speed of the domain wall propagation. This is due to the strong exchange interaction between the spins within a pillar. As shown on Fig. 4.7, the maximum SNR is obtained at a cutting area of $7.5nm \times 7.5nm$ $(3cells \times 3cells)$ because this size is sufficiently large to overcome thermal fluctuations while maintaining coherent rotation within each pillar.

4. Effect of Cellsize:

The storage density can be increased and the operation time for the device decreased if a smaller pillar is used. We tried the element array with cellsize $1.25nm$ and dimension $30.0nm \times 5.0nm \times 5.0nm$ $(24\ cells \times 4\ cells \times 4\ cells)$ under applied fields $0.7Tesla$ and $0.8Tesla$ (Fig. 4.8). The sixteen middle pillars were used to store information. Since the thermal error bars do not overlap each other, a cellsize of $1.25nm$ can be used. With a cellsize of $1.25nm$, an areal storage density of

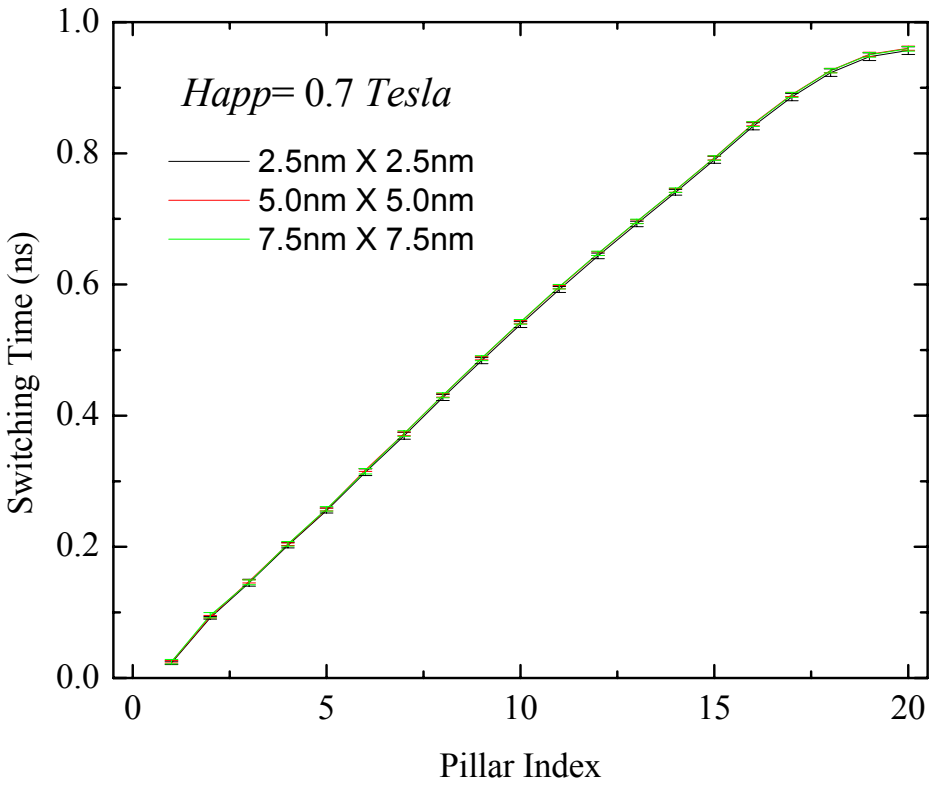

Fig. 4.6 Domain wall propagation with different cutting area

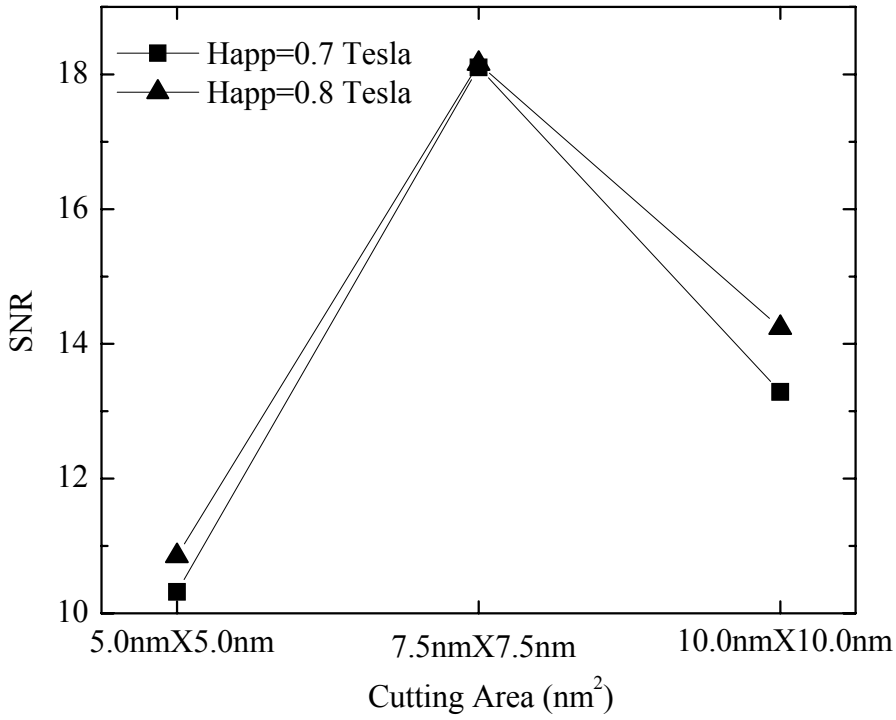

FIG. 4.7 SNR as a function of cutting area

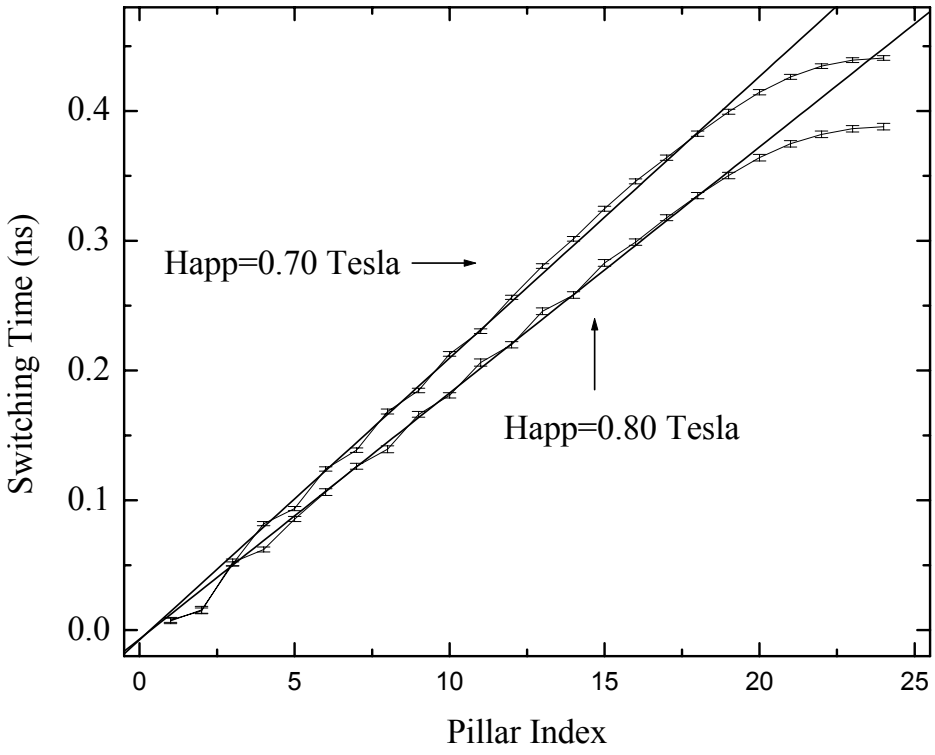

FIG. 4.8 Domain wall propagation with cellsize 1.25*nm*

$2.0 \times 10^4 \, GigaBit / cm^2$ and an operation time to write 4 bits of information of $0.5ns$ can be obtained.

5. Magnetic Reversal by Sinusoidal Field:

In some cases, it may be easier to manipulate the information storage device if the magnetic reversal of the pillars can be controlled by "digital" signals. We simulated digital signals by sinusoidal applied field with period $0.1ns$ and peak magnitude $0.667Tesla$ as given by

$$H_{app} = 0.667 \left| \sin(\frac{\pi}{0.1ns} t) \right| . \qquad \text{(Eq. 4.1)}$$

One period of such an applied field is a reasonable approximation to a field pulse. The sinusoidal field was applied to an element array with cellsize $2.50nm$ and dimension $50nm \times 5nm \times 5nm$ $(20cell \times 2cell \times 2cell)$. The switching times of the pillars were traced and indicated as "•"s on Fig. 4.9. Except for the first and last few pillars, the switching event occurred when the applied field was at its peak and only one pillar switched within each period. This means that a specific number of pillars can be switched as determined by the number of applied periods of the sinusoidal field.

6. Conclusions:

The effects of the magnitude of applied field, cutting area and cellsize of the element array on the "seed" induced domain wall propagation have been studied. Three

different magnetic reversal mechanisms under different applied fields have been investigated. To minimize the effect of thermal noise, external field with magnitude $0.7Tesla$ or $0.8Tesla$ and cutting areas less than $10.0nm \times 10.0nm$ should be used. In such a device, an areal storage density of $2.0 \times 10^4 GigaBit/cm^2$ and operation time for 4 bits of information of $0.5ns$ can be obtained using cellsize of $1.25nm$. A sinusoidal field can also be used to switch a single pillar during each period of the applied field. Our study indicates that the novel method of "seed" induced magnetic reversal can be used to store information that is thermally stable. This stability can be optimized in terms of the external magnetic field and geometry of the element array. Such devices may be viable as a fast, ultra-high density storage medium.

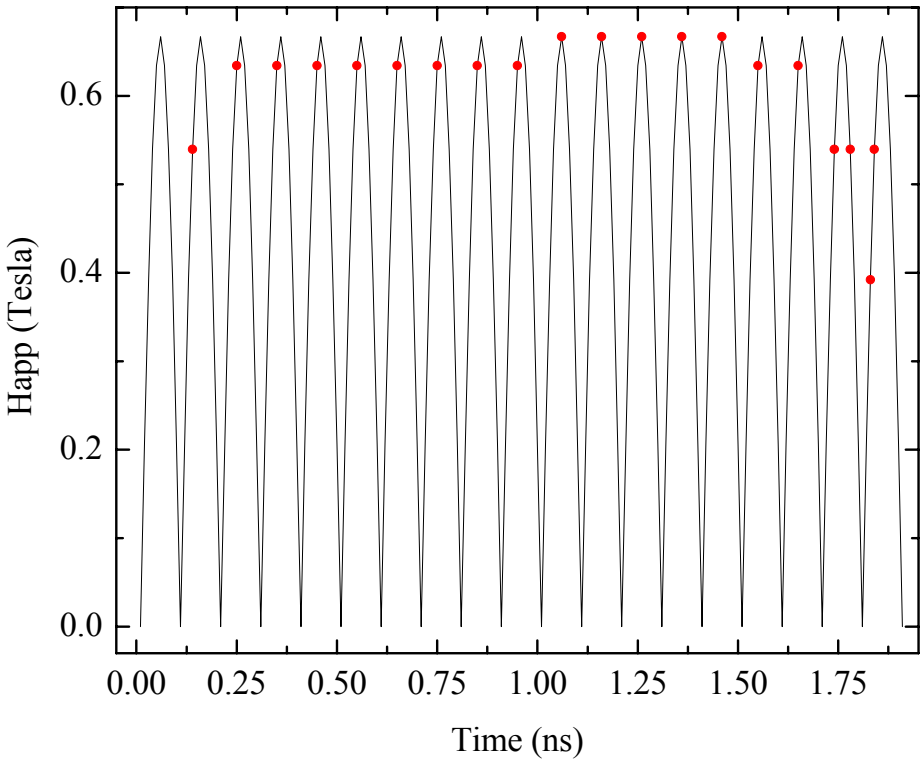

FIG. 4.9 Domain wall propagation under sinusoidal applied field

CHAPTER FIVE: OMMC SYSTEM

OMMC stands for Online MicroMagnetic Calculation. The OMMC system is a project launched in 2002 to develop a stable, easy-to-use and scalable online micromagnetic computation platform for the academic community to calculate spin configuration and hysterisis loops. OMMC is the first web-based platform for micromagnetic calculation. It uses GNU Lesser Public License [33] as its license. OMMC can be used for FREE for academic or educational purposes. Currently, it is located at http://www.linuxdog.net.

1. Architecture of OMMC:

The architecture of OMMC is shown on Fig. 5.1. The OMMC system is a three-tier application that compiles with J2EE [34] (Java 2 Enterprise Edition) standard. J2EE simplifies multitier applications by standardized modular components and a complete set of services to those components. Building on J2EE, the OMMC can use JavaBeans components, Java Servlets API [35], JavaServer Pages [36] and XML [37] technology. The OMMC also takes advantage of many features of the J2SE [38] (Java 2 Standard Edition), such as “Write Once, Run Anywhere” portability and JDBC [39] database access.

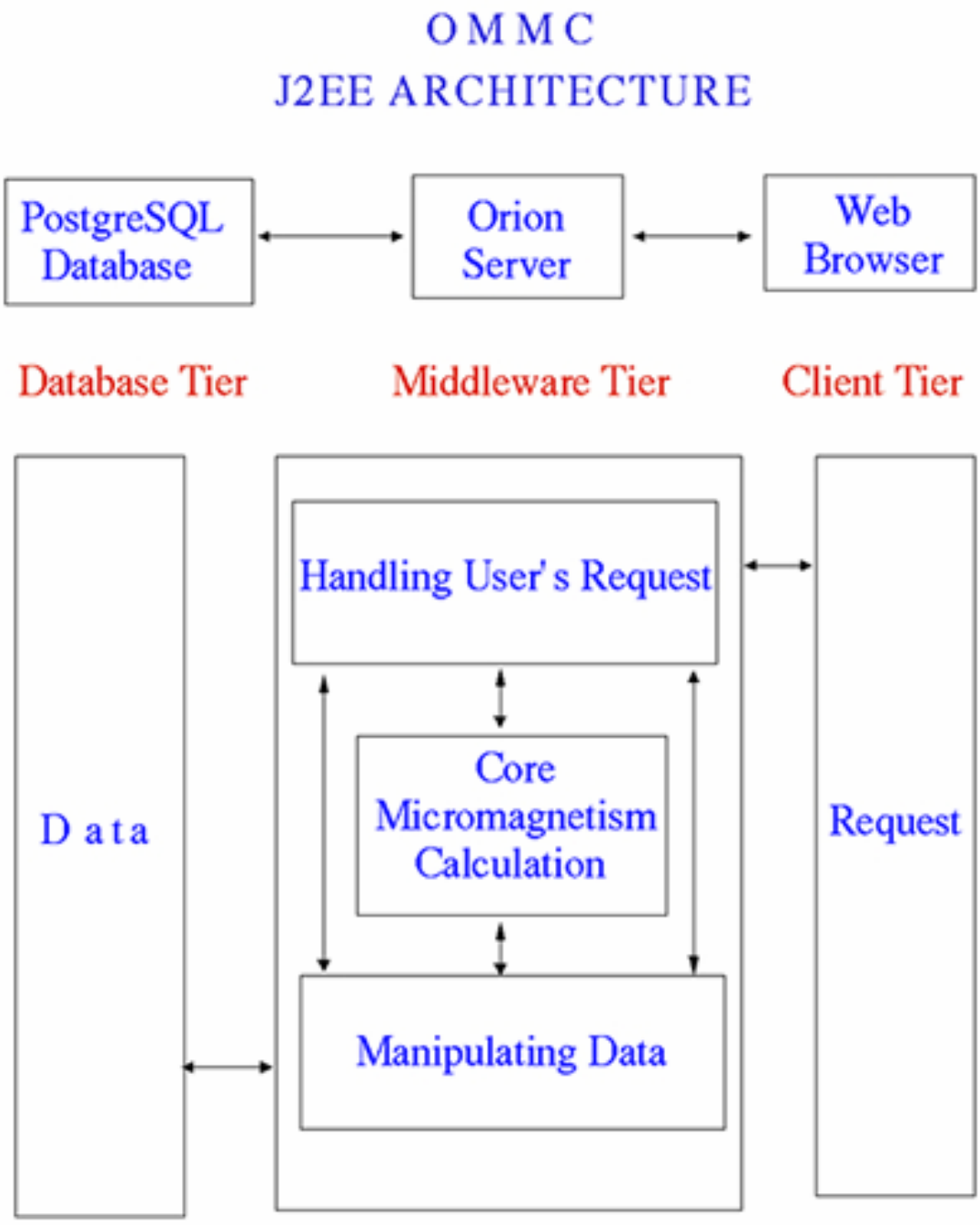

FIG. 5.1 Architecture of OMMC system

The three tiers of the OMMC are database, middleware and client tier. The first two tiers are installed on the server side. The client tier can be any computer that has java-supported web browser installed to communicate with the OMMC server by HTTPprotocol. The client tier handles the user's input of problem definition, sends the calculation request to middleware tire and views the calculation result. The middle tier is the core part of the whole system. The middle tier handles the calculation request sent from the client tier, loads the native code installed on the server to do the calculation and save the calculation results into database located in the database tier. The database tier stores the users' information, the calculation requests and results. The data can be accessed by the middle tier or by any database clients.

2. Client Tier:

Every user should register in the OMMC system before they can log in and use it. As shown on Fig. 5.2, a unique username, a password and an email address are input and stored in the database if the registration is successful. With a registered user account, user can log in the OMMC system (Fig. 5.3). Since the 128-bit SSL [40] (security socket layer) is applied to encrypt and decrypt the data sent between the client browser and web server, the connection between client and server is secure.

After successful login (Fig. 5.4), the user can submit a new calculation request, delete a calculation request that has been done and its calculation results permanently from the database, view the calculation results and check the status of the ongoing calculations. In the module of submitting new request (Fig. 5.5), the material properties

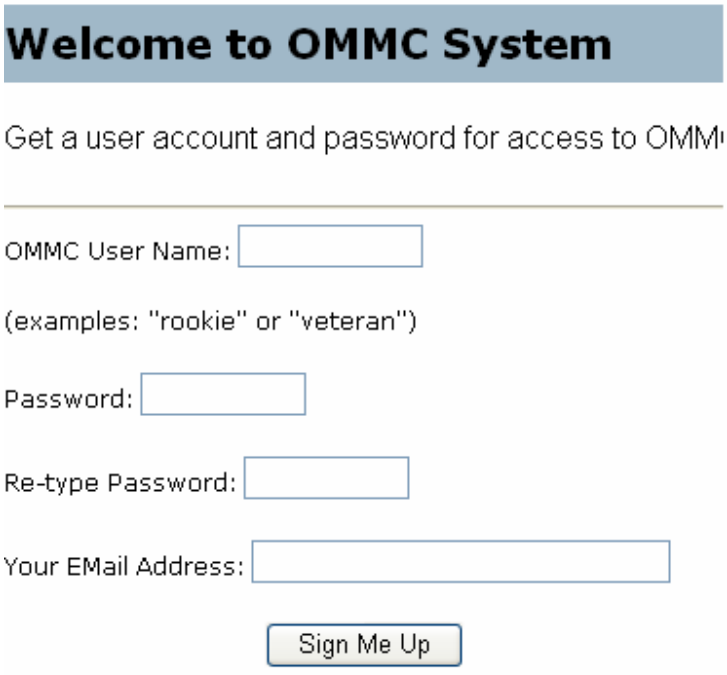

FIG. 5.2 OMMC account registration

FIG. 5.3 User interface to log in OMMC system

and computation control parameters are input in the textfields. Users can choose to press button “Run” to submit it to server or to reset the all the values in the textfields by pressing button “Reset”. In the module of deleting old request (Fig. 5.6), users choose one of the calculation requests from a drop-list and then press button “Delete” to delete it. The command of deleting is permanent and unrecoverable. In the module of viewing calculation result (Fig. 5.7), the calculation request is chosen from the drop-list and the results of it can be displayed in one of the three formats: XML text, 3D model and 2D chart. In the format of XML text (Fig. 5.9), the calculation results are shown as plain XML text that compiles the description of a XML schema. We will discuss the application of XML technology in OMMC in Part 3. In the format of 3D model (Fig. 5.8), the 3D spin configurations are rendered by Java Beans [41] and Java 3D [42] technologies. The user can use computer mouse and keyboard to translate, rotate and scale the 3D models. In the format of 2D chart (Fig. 5.10), hysteresis loops in the X, Y and Z directions are specifically plotted by J4Less [43] technology. In the module of checking status, user can check the status of ongoing calculation request by selecting the request from a drop-list and then pressing button “check”.

The client tier has been tested and runs well for Micrsoft IE 5.0 or up, Netscape 6.0 or up on Windows XP/2000/NT4.0 and Netscape 6.0 or up on Red Hat Linux 7.1, 7.2, 7.3 and 8.0. Sun Microsystem JRE (Java Runtime Environment) 1.3.1_04 or up and Java 3D Runtime Environment 1.2.1 or up are required to be installed properly on the client to support Java2 and Java 3D technologies.

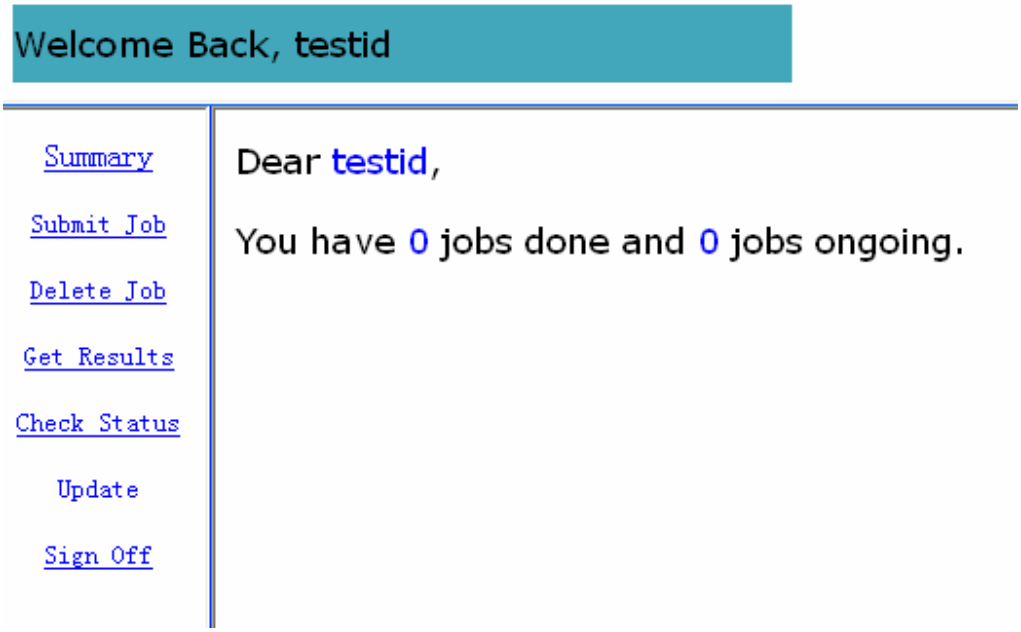

FIG. 5.4 Summary of user account

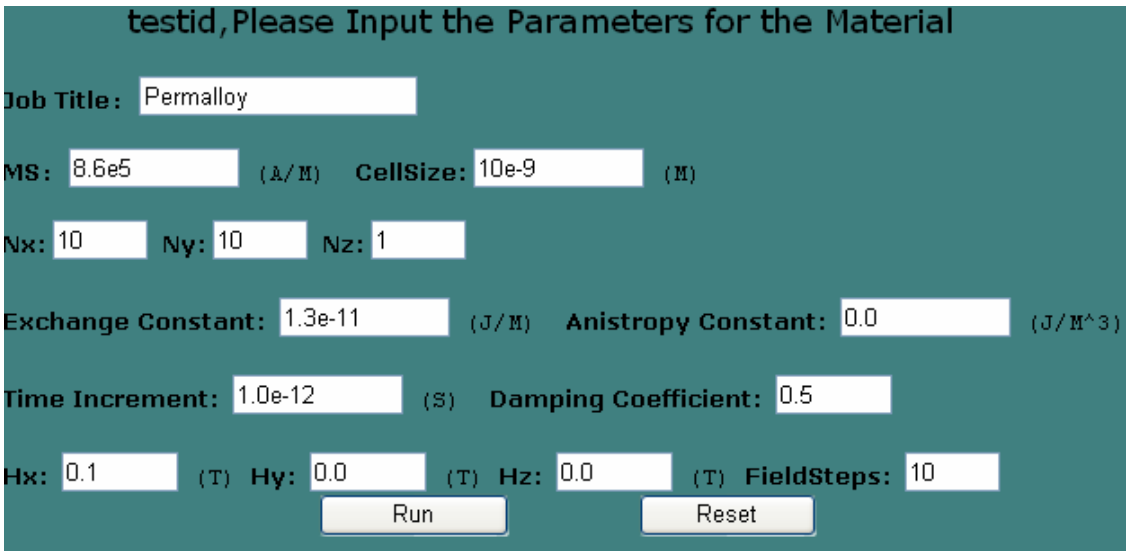

FIG. 5.5 Input of material properties and computation control parameters

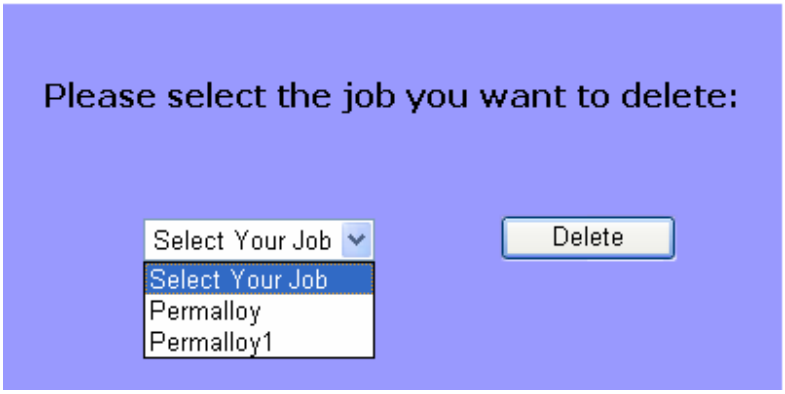

FIG. 5.6 Delete a calculation request

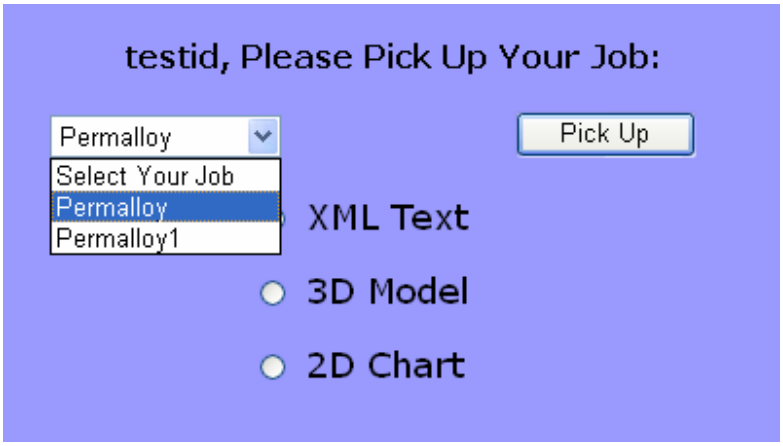

FIG. 5.7. Pick up a calculation request

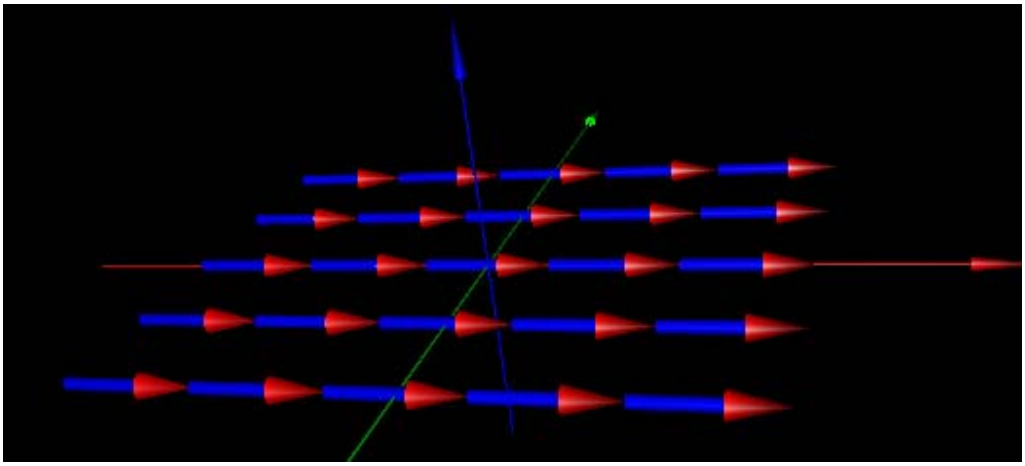

FIG. 5.8 Calculation result in 3D model format

```
<?xml version = "1.0" encoding = "windows-1252"?>
<mmcalculation xmlns="http://www.amri.uno.edu"
xmlns:xsi="http://www.w3.org/2001/XMLSchema-instance"
xsi:schemaLocation="http://137.30.117.3/mmapp/mmschema.xsd">
   <jobinfo>
      <username>testid</username>
      <emailaddress>chenhanning@hotmail.com</emailaddress>
      <jobtitle>Permalloy</jobtitle>
   </jobinfo>
   <control>
      <excon>1.3E-11</excon>
      <ancon>0.0</ancon>
      <ms>860000.0</ms>
      <cellsize>1.0E-8</cellsize>
      <length>5</length>
      <width>5</width>
      <heighth>1</heighth>
      <maxfield>
         <maxfieldx>0.01</maxfieldx>
         <maxfieldy>0.0</maxfieldy>
         <maxfieldz>0.0</maxfieldz>
      </maxfield>
      <fieldstep>10</fieldstep>
      <timestep>1.0E-12</timestep>
```

FIG. 5.9 Calculation result in XML text format

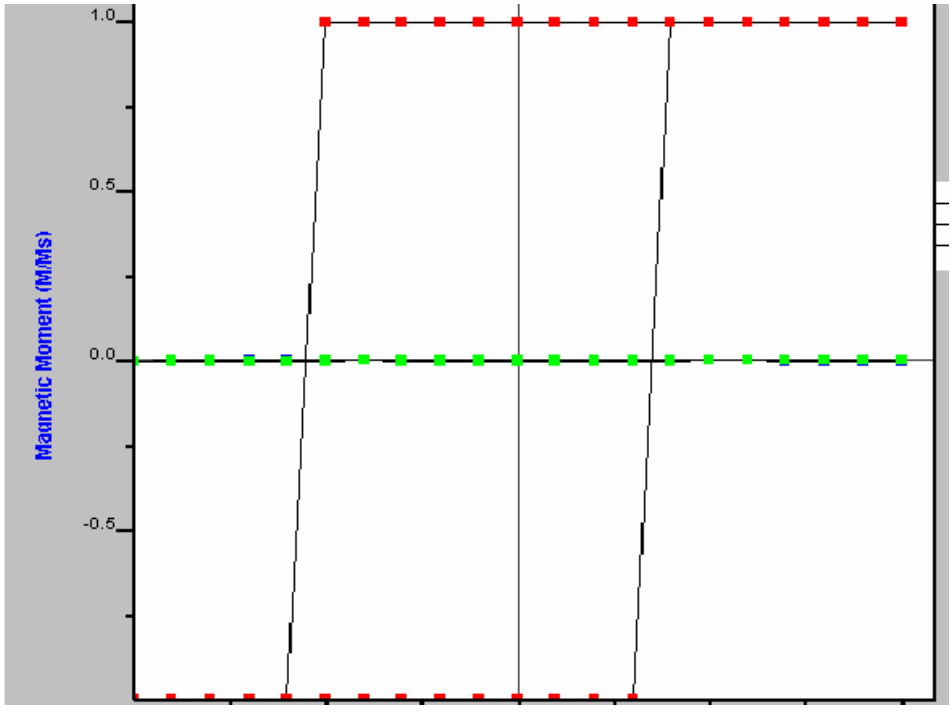

FIG. 5.10 Calculation result in 2D chart format

3. Middleware Tier:

The server side (middlware tier and database tier) is installed on Red Hat Linux 7.3 at a PC with Intel Pentium III 1.0GHz CPU and 256 MB SDRM memory. Orion 1.6.0 [44] is chosen as our J2EE application server to implement the functions of the middleware tier because it fully supports all of the features of J2EE 1.3 and is free for non-commercial download and deployment. The middleware of OMMC communicates with clients by Java Sevlet technology. Based on the client's request, the middleware finds and loads specific Java Enterprise Javabeans to process the client's request and access database tier by JDBC API. Since the Java programming language uses the Virtual Machine to fulfill the feature of platform independence, it usually runs 2 to 10 times slower than the native programming language, such as C, C++ and Pascal which compiles the source code into binary code running directly on CPU rather than the software Virtual Machine for Java. To speed the calculations, some of the expensive computations have been written in C++ and compiled by the GNU C++ 2.96 [45] compiler into native dynamic libraries. The native dynamic libraries can be called from Java middleware by JNI technology. XML stands for Extensible Markup Language. It is a simple text format to provide a flexible way to exchange a great variety of data on the internet or elsewhere. XML schema is for defining the structure, content and semantics of XML document. XML schema [46] is a XML document itself. The OMMC system uses XML technology to store the calculation requests and results into database. The users can handle the requests and display the results in a variety of ways. The XML schema used in the OMMC system is shown in Fig. 5.11.

```
<?xml version="1.0" encoding="UTF-8" ?>
- <xsd:schema xmlns:xsd="http://www.w3.org/2001/XMLSchema"
    targetNamespace="http://www.amri.uno.edu"
    xmlns="http://www.amri.uno.edu"
    elementFormDefault="qualified">
    <xsd:element name="mmcalculation" type="mmcalculationtype"
      />
  - <xsd:complexType name="mmcalculationtype">
    - <xsd:sequence>
        <xsd:element name="jobinfo" type="jobtype" />
        <xsd:element name="control" type="controltype" />
        <xsd:element name="results" type="resultstype" />
      </xsd:sequence>
    </xsd:complexType>
  - <xsd:complexType name="jobtype">
    - <xsd:sequence>
        <xsd:element name="username" type="xsd:string" />
        <xsd:element name="emailaddress" type="xsd:string" />
        <xsd:element name="jobtitle" type="xsd:string" />
      </xsd:sequence>
    </xsd:complexType>
  - <xsd:complexType name="maxfieldtype">
    - <xsd:sequence>
        <xsd:element name="maxfieldx" type="xsd:double" />
        <xsd:element name="maxfieldy" type="xsd:double" />
        <xsd:element name="maxfieldz" type="xsd:double" />
      </xsd:sequence>
    </xsd:complexType>
  - <xsd:complexType name="controltype">
    - <xsd:sequence>
        <xsd:element name="excon" type="xsd:double" />
        <xsd:element name="ancon" type="xsd:double" />
        <xsd:element name="ms" type="xsd:double" />
        <xsd:element name="cellsize" type="xsd:double" />
        <xsd:element name="length" type="xsd:int" />
        <xsd:element name="width" type="xsd:int" />
        <xsd:element name="heighth" type="xsd:int" />
        <xsd:element name="maxfield" type="maxfieldtype" />
        <xsd:element name="fieldstep" type="xsd:int" />
        <xsd:element name="timestep" type="xsd:double" />
      </xsd:sequence>
    </xsd:complexType>
  - <xsd:complexType name="celltype">
    - <xsd:sequence>
        <xsd:element name="mx" type="xsd:double" />
        <xsd:element name="my" type="xsd:double" />
        <xsd:element name="mz" type="xsd:double" />
      </xsd:sequence>
      <xsd:attribute name="x" type="xsd:int" use="required" />
```

```
    <xsd:attribute name="y" type="xsd:int" use="required" />
    <xsd:attribute name="z" type="xsd:int" use="required" />
  </xsd:complexType>
- <xsd:complexType name="cellstype">
  - <xsd:sequence>
      <xsd:element name="cell" type="celltype" minOccurs="1"
        maxOccurs="unbounded" />
    </xsd:sequence>
  </xsd:complexType>
- <xsd:complexType name="avemtype">
  - <xsd:sequence>
      <xsd:element name="avemx" type="xsd:double" />
      <xsd:element name="avemy" type="xsd:double" />
      <xsd:element name="avemz" type="xsd:double" />
    </xsd:sequence>
  </xsd:complexType>
- <xsd:complexType name="resulttype">
  - <xsd:sequence>
      <xsd:element name="exenergy" type="xsd:double" />
      <xsd:element name="anenergy" type="xsd:double" />
      <xsd:element name="zeenergy" type="xsd:double" />
      <xsd:element name="deenergy" type="xsd:double" />
      <xsd:element name="avem" type="avemtype" />
      <xsd:element name="cells" type="cellstype" />
    </xsd:sequence>
    <xsd:attribute name="step" type="xsd:int" use="required" />
    <xsd:attribute name="Hx" type="xsd:double" use="required"
      />
    <xsd:attribute name="Hy" type="xsd:double" use="required"
      />
    <xsd:attribute name="Hz" type="xsd:double" use="required"
      />
  </xsd:complexType>
- <xsd:complexType name="resultstype">
  - <xsd:sequence>
      <xsd:element name="result" type="resulttype"
        minOccurs="1" maxOccurs="unbounded" />
    </xsd:sequence>
  </xsd:complexType>
</xsd:schema>
```

FIG. 5.11 XML Schema

4. Database Tier:

PostgreSQL [47] 7.1.3 is chosen as the database tier because it is a GNU opensource software that can run on all modern Unix-like operation systems, including Linux. It supports SQL99 standard and provides JDBC driver for the Java middletier to access.

5. Features and Limitations of OMMC:

The OMMC is client light since the clients just need a web browser to access the system. It can do realistic 3D micromagnetism calculations including hysterisis loops and save the calculation requests and results using XML format into the database. The users can view the results in either format of XML text, 3D model and 2D chart anytime after calculation is done. The status of the ongoing calculation can also be accessed.

Since OMMC is still in the development stage, it has some limitations. For example, it can only do calculations for homogenous materials with cubic cells and uniaxial anisotropy.

REFERENCES:

1. A. H. Morrish, *the Physical Principles of Magnetism* (John Wiley & Sons, Inc., New York, 1965).

2. S. Chikazumi, *Physics of Ferromagnetism* (Oxford University Press Inc., Oxford, United Kindom, 1997).

3. L. Neel, *Ann. Phys.* (Paris) **17**, 64 (1932).

4. D. J. Craik and R. S. Tebble, *Ferromagnetism and Ferromagnetic Domains* (North-Holland Publishing Company, Amsterdam, Netherland, 1965).

5. A. O. Adeyeye and M. E. Welland, *J. Appl. Phys.* **92**, 8796 (2002).

6. H. Forester, T. Schrefl, D. Suess, W. Scholz, V. Tsiantos, R. Dittrich, and J. Fidler, *J. Appl. Phys.* **91**, 6914 (2000).

7. V. V. Osipov, E. V. Ponizovskaya, and N. Garcia, *Appl. Phys. Lett.* **79**, 2222 (2001).

8. R. P. Cowburn, D. A. Allwood, G. Xiong and M.D. Cooke, *J. Appl. Phys.* **91**, 6949 (2002).

9. A. Zhukov, *Appl. Phys. Lett.* **78**, 3106 (2001).

10. G. Bertotti, *Hysteresis in Magnetism: for Physicists, Materials Scientists and Engineers* (Academic Press, San Diego, 1998).

11. W. F. Brown, Jr., *Phys. Rev.* **130**, 677 (1963).

12. W. F. Brown, Jr., *IEEE Trans. Magn.* **15**, 1196 (1979).

13. W. F. Brown, Jr., *Micromagnetics* (Interscience Publishers, New York, 1963).

14. M. A. M. Haast, J. R. Schuurhuis, L. Abelmann, J. C. Lodder and Th. J. A. Popma, *IEEE Trans. Magn.* **34**, 1006 (1998).

15. D. A. Allwood, Gang Xiong, M. D. Cooke, C. C. Faulkner, D. Atkinson, N. Vernier, R. P. Cowburn, *Science* **296**, 2003 (2002).

16. R. P. Cowburn, M. E. Welland, *Science* **287**, 1466 (2000).

17. R. H. Koch, G. Grinstein, G. A. Keefe, Lu. Yu, P. L. Trouilloud, W. J. Gallagher, S. S. P. Parkin, *Phys. Rev. Lett.* **84**, 5419 (2000).

18. E. Girgis, J. Schleten, J. Shi, J. Janeski, S. Tehrani, H. Goronkin, *Appl. Phys. Lett.* **76**, 3780 (2000).

19. L. Torres, L. Lopez-Diaz, O. Alejos, J. Iniguez, *Physica B* **275**, 59 (2000).

20. R. P. Cowburn, *J. Phys. D.* **33**, R1 (2000).

21. M. Herrmann, S. McVitie, and J. N. Chapman, *J. Appl. Phys.* **87**, 2994 (2000).

22. J. Shi, S. Tehrani and M. R. Scheinfein, *Appl. Phys. Lett.* **76**, 2588 (2000).

23. L. Torres, E. Martinez, L. Lopez-Diaz, and J. Iniguez, *J. Appl. Phys.* **89**, 7585 (2001).

24. Y. B. Xu, C. A. F. Vaz, A. Hirohata, C. C. Yao, W. Y. Lee, J. A. C. Bland and F. Rousseaux, E. Cambril, and H. Launois, *J. Appl. Phys.* **85**, 6178 (1999).

25. H.-N. Lin, Y. H. Chiou, B.-M. Chen H.-P. D. Shieh and Ching-Ray Chang, *J. Appl. Phys.* **83**, 4997 (1998).

26. R. Jansen, O. M. J. van 't Erve, S. D. Kim, R. Vlutters, P. S. Anil Kumar, and J. C. Lodder, *J. Appl. Phys.* **89**, 7431 (2001).

27. N. Dao, S. L. Whittenburg, Y. Hao, C. A. Ross, L. M. Malkinski, and J. Q. Wang, *J. Appl. Phys.* **91**, 8293 (2002).

28. T. Ono, H. Miyajima, K. Shigeto, K. Mibu, N. Hosoito, and T. Shinjo, *J. Appl. Phys.* **85**, 6182 (1999).

29. H. Schmidt, *J. Appl. Phys.* **93**, 2107 (2003).

30. H. Forster, T. Schrefl, D. Suess, W. Scholz, V. Tsiantos, R. Dittrich, and J. Fidler, *J. Appl. Phys.* **91**, 6914 (2002).

31. N. Hayashi, K. Saito and Y. Nakatani, *Jpn. J. Appl. Phys.* **35**, 6065 (1996).

32. W. H. Press, B. P. Flannery, S. A. Teukolsky, W. T. Vetterling, *Numerical Recipes in C : The Art of Scientific Computing* (Cambridge University Press, Cambridge, United Kingdom, 1993).

33. http://www.gnu.org/licenses/licenses.html

34. http://java.sun.com/j2ee/

35. http://java.sun.com/products/servlet/

36. http://java.sun.com/products/jsp/

37. http://www.w3.org/XML/

38. http://java.sun.com/j2se/

39. http://java.sun.com/products/jdbc/

40. http://wp.netscape.com/eng/ssl3/

41. http://java.sun.com/products/javabeans/

42. http://java.sun.com/products/java-media/3D/

43. http://www.java4less.com/

44. http://www.orionserver.com/

45. http://gcc.gnu.org/

46. http://www.w3.org/XML/Schema/

47. http://www.postgresql.org/

VITA

Hanning Chen was born in Beihai City, GuangXi, People's Republic of China. He finished his undergraduate study at Department of Polymer Science and Engineering, University of Science and Technology of China (USTC) and received the Bachelor of Science degree in 1999. In 2000, he came to the United States to pursue his graduate degree at Department of Chemistry, University of New Orleans.

THESIS EXAMINATION REPORT

CANDIDATE: Hanning Chen

MAJOR FIELD: Physical Chemistry

TITLE OF THESIS: Micromagnetics Study of "Seed" Induced Incoherent Magnetic Reversal in a Cobalt Element Array

APPROVED:

Major Professor & Chair -

Dean of the Graduate School

EXAMINING COMMITTEE:

DATE OF EXAMINATION: April 29, 2003